Journal of CO2 Utilization 65 (2022) 102238

Contents lists available at ScienceDirect

Journal of CO2 Utilization

journal homepage: www.elsevier.com/locate/jcou

# 2D/2D $V_2C$ mediated porous g-$C_3N_4$ heterojunction with the role of monolayer/multilayer MAX/MXene structures for stimulating photocatalytic $CO_2$ reduction to fuels

Mohamed Madi [a], Muhammad Tahir [b,*], Zaki Yamani Zakaria [a]

[a] *School of Chemical and Energy Engineering, University Technologi Malaysia, 81310 Johor Bahru, Malaysia*
[b] *Chemical and Petroleum Engineering Department, UAE University, P.O. Box 15551, Al Ain, United Arab Emirates*

## ARTICLE INFO

*Keywords:*
$CO_2$ photoreduction
Vanadium carbide MXenes
g-$C_3N_4$
Solar fuels

## ABSTRACT

2D vanadium carbide ($V_2C$) MXene nanosheets coupled 2D porous g-$C_3N_4$ (PCN) was designed and tested for photocatalytic $CO_2$ reduction under visible light. Controlled coupling g-$C_3N_4$ with $V_2C$ MXene resulted in higher visible light absorption and efficient charge separation. Comparatively, $V_2C$ MXene found more favorable than $V_2AlC$ MAX due to more proficient charge separation. Highest performance was achieved with optimized 15%-$V_2C$/g-$C_3N_4$, in which CO and $CH_4$ generation rates of 151 and 205 μmol $g^{-1}$, respectively, were attained. This enhancement was significantly higher than using $V_2AlC$/g-$C_3N_4$ and pure g-$C_3N_4$ samples due to higher conductivity and large $CO_2$ adsorption capacity. The performance of $V_2C$/g-$C_3N_4$ composite was further examined under a variety of conditions such as pressure, catalyst loading, and reducing agents. With increasing pressure, higher yield of CO and $CH_4$ was attained due to increased reactant adhesion to the catalyst surface, whereas increasing catalyst loading has adverse effects. Water was the best reducing agent for CO evolution, while the methanol–water system enhanced $CH_4$ generation. Furthermore, the stability of composite lasted for several cycles without showing any obvious deterioration. The potential outcomes are assigned to a porous structure with intimate contact, effective charge carrier separation and porous 2D g-$C_3N_4$ transporting electrons towards MXene surface. This study shows that 2D $V_2C$ MXene could be a potential carrier for constructing 2D/2D heterojunctions in photocatalytic $CO_2$ reduction to produce useful solar fuel.

## 1. Introduction

Fossil fuels emit carbon dioxide ($CO_2$) into the atmosphere, which is a main contributing factor to global warming and climate change. Therefore, solar energy is regarded as one of the most successful and promising alternatives for addressing existing environmental issues while also meeting rising energy demand [1,2]. Using photo-technology is a potential approach for turning solar energy into chemical energy [3]. The photocatalytic conversion of $CO_2$ permits the generation of valuable products such as carbon monoxide, methane and methanol, formaldehyde and formic acid in a single process step [4,5]. It was therefore necessary to presence light energy, a high-performance catalyst, and low-cost feedstock ($CO_2$ and water) in order to complete the process successfully [6]. Several research efforts have been conducted to develop efficient photocatalysts for the reduction of $CO_2$ such as $TiO_2$ [7], $ZnV_2O_4$ [8], $WO_3$, and CdS [9]. However, the efficiency of photocatalytic $CO_2$ reduction is still lagged far behind the requirement of practical applications [10].

Two-dimensional (2D) nanomaterials have sparked widespread interest in the photocatalysis field since their discovery [11]. This is due to their unique physicochemical properties, which include a large surface area, a higher carrier separation rate, a broad optical absorption spectrum, low cost, several surface-active spots, and so forth [12,13]. Finding efficient 2D materials with a suitable band gap and excellent photoelectric properties as ideal photocatalysts is critical from the standpoint of the photocatalytic process. A variety of 2D structured materials have been investigated in recent years [14]. Among them, graphitic carbon nitride (g-$C_3N_4$) as a noble metal-free material is a promising alternative due to its high stability with a low cost, ease of preparation, increased reduction potential, and good photocatalytic performance under visible light [15–17]. However, the photocatalytic activity of g-$C_3N_4$ is lower because it has a higher recombination rate

---

* Corresponding author.
*E-mail addresses:* muhammad.tahir@uaeu.ac.ae, bttahir@yahoo.com (M. Tahir).

https://doi.org/10.1016/j.jcou.2022.102238
Received 28 May 2022; Received in revised form 14 September 2022; Accepted 17 September 2022

and less specific surface area [18]. Several techniques for increasing g-$C_3N_4$ activity for selective $CO_2$ reduction have been investigated. This comprises surface modification, metal loading, O-doping, and interaction with other photocatalysts [19,20]. For example, Mg/g-$C_3N_4$, $WO_3$/g-$C_3N_4$ and $Cu_2V_2O_7$/g-$C_3N_4$ have been used for $CO_2$ reduction to produce CO and $CH_4$ [21]. There have also been attempts to increase the activity of g-$C_3N_4$ by employing metal/semiconductor composite systems, but these systems are ineffective and uneconomical because of the high cost of metals [22]. Fortunately, the activity of g-$C_3N_4$ could also be increased when it is combined with noble metal-free materials as a co-catalyst and/or mediator with the layered structure [23].

MXenes, comprising transition metal carbides, nitrides, and carbonitrides, are a novel family of two-dimensional (2D) materials that have gained considerable attention in recent years [24]. MXenes, like vanadium carbide ($V_2C$) MXene are newly explored layered materials which have several distinctive properties such as excellent electrical conductivity, great structural stability, and efficient absorption of visible light [25,26]. Theoretically,$V_2C$ MXene shows improved performance in different applications especially as electrode material (both of cathode and anode) [27], energy storage [10], batteries [28], magnetic shielding [29,30], and catalysis [31,32], and $CO_2$ capture [25,33]. As a result, it is possible to decorate $V_2C$ MXene with semiconductors that could provide remarkable photocatalytic activity, which provides a new possibility for cost-effective alternatives to the noble metal [34–36]. Therefore, they are potential candidates to replace noble metal catalysts for photocatalytic $CO_2$ reduction reaction.

In order to create 2D/2D heterojunction photocatalysts based on g-$C_3N_4$, various research have concentrated on hybridizing g-$C_3N_4$ with other 2D materials. The intimate interaction contact in a 2D/2D heterojunction provides a significant contact area and a lot of pathways for the migration and separation of charge carriers produced by photons. Moreover, the 2D/2D heterojunction inherits the advantages of the 2D structure, such as high specific surface area, plentiful adsorption sites, and active sites [37]. More importantly, 2D $V_2C$ MXene can be combined with other semiconductors materials to develop Schottky junction, which effectively promotes charge carrier separation. As a result, the utilization of $V_2C$ in the photocatalysis field is predicted to increase the yield and selectivity [38]. Previously, several studies have been done to increase the photoactivity of $CO_2$ reduction using $Ti_3C_2$ MXene [26,39,40]. For example, Tang et al. prepared alkalinized MXene $Ti_3C_2$ coupled g-$C_3N_4$ and observed an increase in photoactivity for CO/$CH_4$ synthesis during the $CO_2$ photoreduction process [23]. Likewise, a 2D/2D heterojunction of $Ti_3C_2$/g-$C_3N_4$ demonstrated improved photocatalytic hydrogen generation [41]. In another study, Lu et al. constructed a 2D/2D g-$C_3N_4$/$BiVO_4$ heterojunction for $CO_2$ reduction and reported that connecting g-$C_3N_4$ with $BiVO_4$ increases $CO_2$ reduction activity [42]. According to Zhu et al., loading $Ti_3C_2$ quantum dots improved the $CO_2$ reduction efficiency of the 2D/2D $TiO_2$/$C_3N_4$ composite [43]. As a result, $Ti_3C_2$ MXene offers new routes for constructing high efficiency nanocomposite systems for enhancing photocatalytic $CO_2$ reduction by employing solar light [44]. Although $V_2C$ has more distinctive characteristics than $Ti_3C_2$, this is because vanadium surface layers of $V_2C$ could potentially permit pseudocapacitive behavior compared to $Ti_3C_2$ MXene, which has numerous oxidation states of V ion [45]. Furthermore, vanadium can offer several oxidation states, which can render a broad range of redox reactions. This could enhance electrical conductivity, mechanical characteristics, and reactivity. More importantly, this can promote charge transfer between the adsorbate and $V_2C$ support [46]. This could make $V_2C$ MXene more appealing for photocatalysis when it is taken into consideration the good electrical conductivity and better performance [47,48]. It is also possible to hypothetically create a Schottky junction with the use of metals that have greater work functions than an n-type semiconductor. Thus, $V_2C$ MXene can be considered more efficient than $Ti_3C_2$ MXene and other MXenes [25,33]. Moreover, due to the fact that the work function of the $V_2C$ MXene electrode material is greater than that of g-$C_3N_4$, it is possible to build a 2D/2D $V_2C$/g-$C_3N_4$ heterojunction composite by combining them. Thus, it would be able to achieve high light absorption and improved charge carrier separation [41,49]. More interestingly, there is no report available for the utilization of $V_2C$ MXene in photocatalytic $CO_2$ reduction applications. A significant benefit of the creation of a 2D/2D heterojunction has the potential to improve catalytic activity for maximizing charge separation. Thus, it would be able to achieve high light absorption and improved charge carrier separation [41,49].

In the present study, newly designed 2D/2D $V_2C$ MXene coupled g-$C_3N_4$ nanosheet heterojunction with Schottky junction was successfully developed for efficient photocatalytic $CO_2$ reduction to fuels under visible light with the enhanced interfacial transfer of photogenerated charges in the composite material. The best results were observed with 15%-$V_2C$/g-$C_3N_4$ composite and was favorable for boosting $CO_2$ methanation. Furthermore, considerable selectivity changes were found, with the addition of $V_2C$, which boosting the selectivity of the $CH_4$ formation. The role of different reforming systems such as $CO_2$ reduction with water, hydrogen and methanol was critically examined to understand their impacts on products yield and selectivity. The performance of the composite was further investigated under different operating parameters such as pressure, time and catalyst loading. The stability analysis was carried out in a series of cycles in order to monitor the life of the catalyst. Finally, the possible mechanism for the photocatalytic $CO_2$ reduction over the $V_2C$/g-$C_3N_4$ composite has been proposed. As far as we know, there is no report on the use of 2D/2D $V_2C$/g-$C_3N_4$ heterojunction material in photocatalytic $CO_2$ reduction to produce solar fuels under visible light irradiation. As a result, our research paves the way for the development of a highly efficient and sustainable 2D/2D heterojunction system capable of significantly increasing photocatalytic conversion of $CO_2$ to solar fuels.

## 2. Experimental

### 2.1. Chemicals

The synthesis of graphitic carbon nitride was carried out using melamine (Sigma Aldrich, AR $\geq$ 99%) while $V_2AlC$ (>98%, 200 mesh, Famous Chem China) has been used to synthesize $V_2C$ MXene. The chemicals used are Methanol (95%, Sigma Aldrich), Hydrofluoric acid (HF, 49%, Emplura) and Deionized water (DI).

### 2.2. Synthesis of g-$C_3N_4$ porous structure

The hydrothermal approach was used to synthesize g-$C_3N_4$ using melamine as a precursor [16,50]. First, (5 g) of melamine was placed in a ceramic crucible, covered with a lid, and heated in a furnace at 550°C for 2 h in an air atmosphere. The fine powder was obtained by grinding the bulk g-$C_3N_4$ in a mortar and pestle. The resultant g-$C_3N_4$ powder was distributed in 20 mL methanol and agitated for 24 h before being ultrasonically treated for 30 min to yield highly scattered g-$C_3N_4$ nanosheets. Lastly, 2D g-$C_3N_4$ nanosheets were obtained by drying samples in an oven at 80°C under air atmosphere.

### 2.3. Synthesis of $V_2C$ MXene

The $V_2C$ MXene nanosheets was synthesized through etching $V_2AlC$ with HF solution (content $\geq$ 49%) in a continuous stirred tank reactor to remove the Al atoms layers [26]. The main process of fabricating $V_2C$ MXene is shown in Fig. 1. Firstly, (1 g) $V_2AlC$ (powder) was added to a 20 mL HF solution (49% concentration) in Teflon-lined reactors and magnetically swirled for 48 h at room temperature. Subsequently, all MXenes suspension was transferred into a separate beaker and washed with deionized water, and centrifuged until the pH value of the supernatant reached ~6. The different etching times of $V_2C$ (12, 24, and 48 h) was investigated for photocatalytic $CO_2$ reduction. The best etching time of $V_2C$ MXene was at 48 h. Afterward, the product was dried at 100°C for

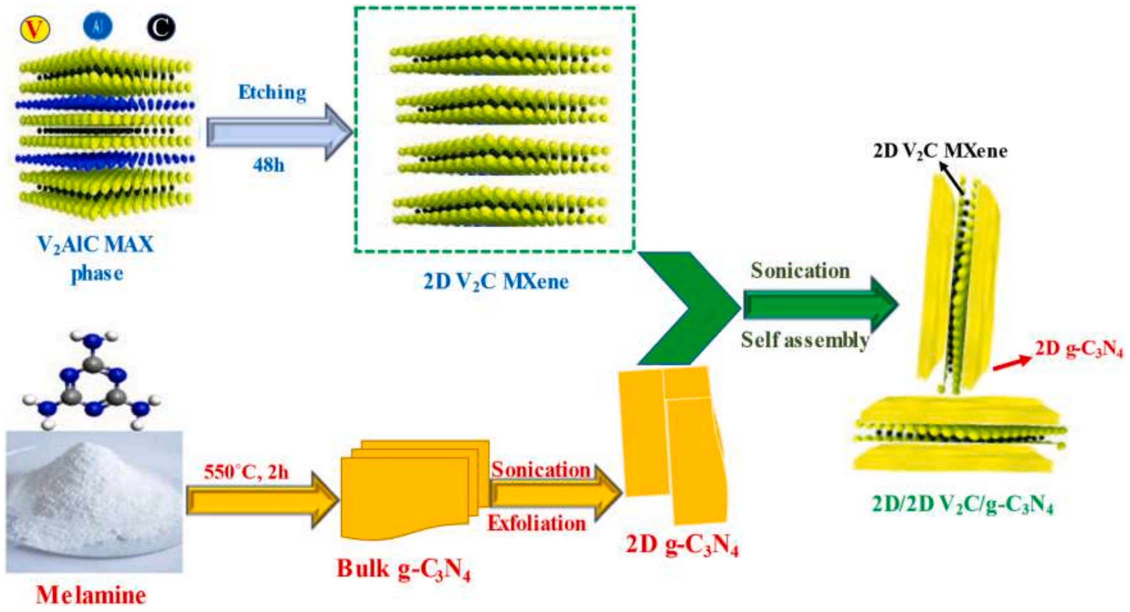

**Fig. 1.** Schematic illustration of $V_2C$/g-$C_3N_4$ nanocomposite preparation.

48 h in an oven with regulated airflow and was designated as $V_2C$ MXenes nanosheets at the etching time (48 h).

### 2.4. *Synthesis of 2D/2D $V_2C$/g-$C_3N_4$*

For the construction of 2D/2D $V_2C$/g-$C_3N_4$ nanosheets composite, physical mixing followed by an ultrasonic approach was employed. Typically, a specific amount of g-$C_3N_4$ nanosheets (1 g) was dispersed in (20 mL) methanol solution and stirred for 6 h. Following that, specific amounts of $V_2C$ MXene nanosheets (0.15 g) were dispersed into beaker of methanol (20 mL) and stirred for 6 h as well. Afterward, $V_2C$ MXene nanosheets was gradually added to the g-$C_3N_4$ nanosheets dispersion and agitated for an additional 12 h to obtain a well-dispersed 2D/2D $V_2C$/g-$C_3N_4$ heterojunction composite. The final products were dried at 100°C overnight to obtain $V_2C$/g-$C_3N_4$ nanosheets composite. The different amounts of $V_2C$ (5, 10, 15, and 20 wt%) were also coupled with g-$C_3N_4$. The scheme for the preparation of $V_2C$ loaded g-$C_3N_4$ and their composites have been presented in Fig. 1.

### 2.5. *Characterization of materials*

The crystalline phase and structural of the photocatalysts were determined using X-ray diffraction (XRD); Diffraction was carried out utilizing Bruker Advance D8 diffractometer, which is capable of operating at 40 kV, 40 mA, and a Cu K radiation source. The Raman and Photo-luminance (PL) analyses were performed using a Raman Spectrometer (Lab RAM HR Evolution, HORIBA) with laser emission wavelengths of 532 and 325 nm, respectively. Raman analysis was utilized to determine rotational, vibrational, and other low-frequency patterns of photocatalysts, whereas, the effects of rate of recombination of the these photocatalysts were investigated using photoluminescence (PL). Microstructures and surfaces were examined using a Field Emission Scanning Electron Microscope (FE-SEM, Hitachi SU8020), while elemental composition and mapping investigations were carried out using Energy Dispersive X-ray spectroscopy (EDX). For light absorption and band gap estimates, diffuse reflectance spectra (DRS) in the ultraviolet-visible (UV–vis) range were acquired using UV–vis spectrophotometer (Perkin Elmer, LAMDA 365). Electrochemical experiments were made with 0.1 M $Na_2SO_4$ in an electrode system consisting of Pt wire, Ag/AgCl electrode, and sample electrode (reference electrode) using an electrochemical workstation (CHI660E).

### 2.6. *Photocatalytic activity test*

The efficiency of photocatalysts was examined using a photoreactor in the gaseous phase within the irradiation range of visible light. The photoreactor is made up of a stainless-steel cylindrical vessel with total volume 80 $cm^3$ and a length of 5 cm. It was supplied with a 10 mm thick Pyrex glass for passing the light, as well as a parabolic-shaped reflector was utilized to direct light inside the photoreactor room. Visible light was used with a power output of (20 $mW/cm^2$), which was a 35 W HID Xe lamp. Typically, a specific quantity of powder photocatalyst (50 mg) was spread uniformly throughout the reactor at a distance of roughly 6 cm, directly facing the lamp. The experiments were conducted using different catalyst loading: 25, 50, 100, and 150 mg to determine the impact of catalyst loading. The reactor was purged continuously by mixture of $CO_2/H_2O$ to remove any unwanted gases prior to start the experiments. After that, at a steady flow rate of 20 mL $min^{-1}$, compressed high quality of carbon dioxide (99.9%) was bubbling via water at 25°C, causing the water vapor to be transferred into the photoreactor chamber together with the $CO_2$ gas. To begin the photocatalytic $CO_2$ reduction process, the input and output vents were sealed and the source of light was turned on, resulting in the creation of CO and $CH_4$ gases via a series of redox processes. In the end, gas products were collected at regular intervals after using a gastight syringe (Agilent, 1000 L) for offline analysis. A Gas Chromatograph was used to analyze the gas products (GC, 6890). Two detectors, a flame ionization detector (FID) and a thermal conductivity detector (TCD), as well as a Carboxen 1010 PLOT capillary column, were included in the gas chromatograph.

## 3. Results and discussion

### 3.1. *Characterization of materials*

#### 3.1.1. *X-ray diffraction (XRD)*

The binary 15%-$V_2C$/g-$C_3N_4$ nanocomposite was analyzed using X-ray diffraction to determine the crystalline structure and the presence of all catalyst components and the results are shown in Fig. 2(a). The bulk $V_2AlC$ MAX were verified to have a hexagonal crystal structure. The diffraction peaks at 13.5°, 27.2°, 36.2°, 41.4°, 45.3°, 55.6°, 64°, 76°, and 79° were attributed to the crystal indices of the (002), (004), (101), (103), (104), (106), (110), (109), and (116) planes in hexagonal $V_2AlC$, where the MAX phase of $V_2AlC$ is linked to the normal peak (JCPDS Card No.

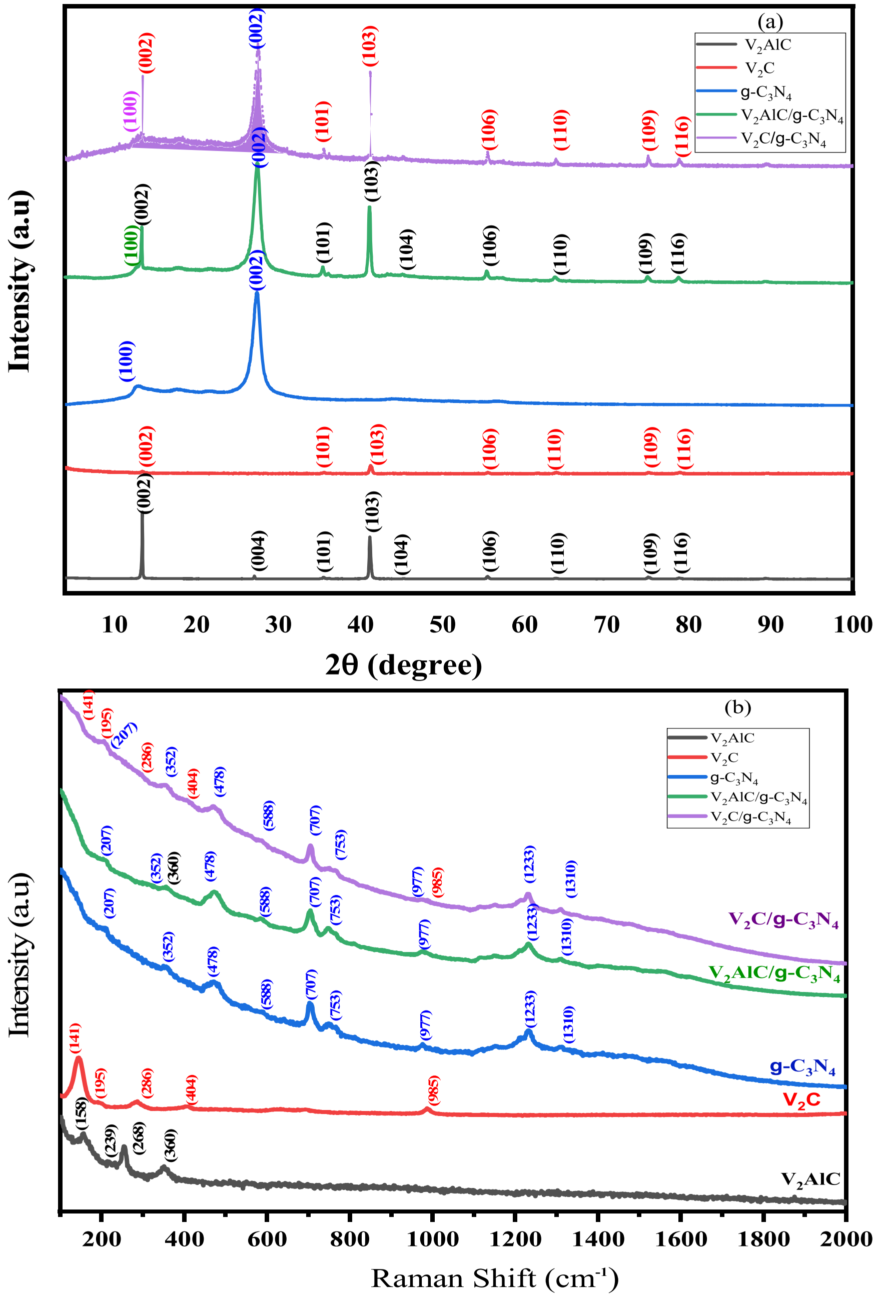

**Fig. 2.** (a) XRD patterns of $V_2AlC$, $V_2C$, g-$C_3N_4$, 10%$V_2AlC$/g-$C_3N_4$ and 15%-$V_2C$/g-$C_3N_4$; (b) Raman spectra of $V_2AlC$, $V_2C$, g-$C_3N_4$, 10%$V_2AlC$/g-$C_3N_4$ and 15%-$V_2C$/g-$C_3N_4$ samples.

29–0101) [51–53]. After etching of $V_2AlC$ with HF, $V_2C$ MXene nanosheets were formed. A hexagonal crystal structure was found in the $V_2C$ MXene after it was etched and exfoliated. The strongest peaks almost vanish completely after HF etching, showing that the $V_2AlC$ to $V_2C$ MXene structure was successfully converted. The diffraction angles at 13.4°, 35.5°, 41.4°, 55.6°, 63.7°, 75°, and 79° were assigned to the crystal indices of (002), (101), (103), (106), (110), (109), and (116) of the delaminated $V_2C$ MXene [54]. For the exfoliated few-layer $V_2C$ nanosheets, the peaks at 13.4° sand 41.4° are complete significantly disappeared, confirming the completely removal of Al atoms and an increase of c-lattice parameter of few-layer $V_2C$ [46]. The peaks at 75° and 79° agreed well with the (109) and (116) crystal planes of $V_2AlC$ respectively, which confirm the successful synthesis of $V_2C$ nanosheet from bulk $V_2AlC$. An important distinctive peak of the g-$C_3N_4$ was observed at 2θ:13°, which corresponds to (100) diffract plane, which indicates the graphitic carbon nitride aromatic systems interlayer structural packing. There is also a significant peak centered at 2θ:27.5° that corresponds to the plane (002) (JCPDS card No. 87–1526) [55], which is known as the distinctive interplanar stacking peak, and which has an interlayer distance of 0.326 nm [56]. It is worth mentioning that no impurity was observed in the primary peaks of either the $V_2AlC$ MAX/g-$C_3N_4$ or the $V_2C$ MXene/g-$C_3N_4$ samples. This demonstrates the efficient synthesis of both nanocomposite catalysts, as evidenced by their effective interaction.

### 3.1.2. *Raman spectroscopy*

The Raman spectroscopy have been used to identify interactions between the components in the composite sample, and the results are presented in Fig. 2(b). The formation of the polymeric structure of g-$C_3N_4$ was evident as peaks were found at 207,352, 478, 588, 707, 753, 977, 1233, and 1310 $cm^{-1}$, suggesting that the polymers pattern of g-$C_3N_4$ was generated, which is largely corresponds previously reported literature for pure g-$C_3N_4$ [18,57]. Vibration causes three Raman peaks in the tri-s-triazine ring (478, 707, and 1233 $cm^{-1}$). Furthermore, the presence of heptazine ring pattern was verified by the presence of observable peaks at 707 and 977 $cm^{-1}$. Graphitic carbon was also responsible for the C-N stretching vibration and the D and G bands. This could be identified by the presence of broad asymmetric peaks spanning 1300–1700 $cm^{-1}$ [22]. As a result, thermal decomposition of melamine at 550°C is a preferred temperature for the entire poly-condensation process in order to obtain a pure g-$C_3N_4$ structure. The bulk $V_2AlC$ MAX shows distinct Raman peaks at 158, 239, 258, and 360 $cm^{-1}$. The Raman vibrations at 158 and 239 $cm^{-1}$ ($E_{2\,g}$) are used to represent the in-plane vibrations of V and Al atoms, while the vibrations at 258 $cm^{-1}$ ($E_{1\,g}$) and 360 $cm^{-1}$ ($A_{1\,g}$) indicate the in-plane and out-of-plane vibrations of the V atom [58]. Contritely, the Raman spectra of $V_2C$ powder contained a large peak at 141 $cm^{-1}$ and additional minor peaks at 195, 268, 404, and 985 $cm^{-1}$, all of which could be attributed to the Raman-active vibration modes $\omega_1$, $\omega_2$, $\omega_3$, $\omega_4$, and $\omega_5$, which corresponded to the previously studies $V_2C$ vibration mode [33,59]. A partially un-etched $V_2AlC$ area could be assigned to the Raman peak at 268 $cm^{-1}$. This proves the conversion to MXene and enables the monitoring of the Raman signature at a given location as a function of etching time [60]. Additionally, a new peak at the frequency (985 $cm^{-1}$) appears, which is most likely due to the enhanced interlayer spading in $V_2C$ MXene compared to bulk $V_2AlC$. The peak at 404 $cm^{-1}$ has been attributed to the active vibration modes of the terminated $V_2C$ MXene. In general, the Raman findings prove that $V_2C$ MXene has been synthesized successfully and all these peaks begin to appear as a result of the increased etching time of bulk $V_2AlC$ [27]. By comparing the two peaks of 195 and 286 $cm^{-1}$ in the composite of $V_2C$-g-$C_3N_4$, it can be concluded that $V_2C$ has been successfully integrated into the composite. Furthermore, the obvious $V_2C$ peak at 985 $cm^{-1}$ further established the presence of $V_2C$ in the $V_2C$-g-$C_3N_4$ composite. The strong interaction between $V_2C$ and g-$C_3N_4$ results in a strong chemical coupling that enables the $V_2C$-g-$C_3N_4$ composites to have an extreme conductivity for the transfer of electron. All of these findings indicate that the $V_2C$-g-$C_3N_4$ composite was successfully synthesized with good components interaction to form a heterojunction.

### 3.1.3. Photoluminescence (PL) analysis

To identify the optical features of semiconductor nanomaterials, the use of Photoluminescence (PL) analysis is an efficient approach in particular, in obtaining information regarding surface oxygen vacancies and the separation of photogenerated charges. PL analysis can be used to assess the recombine of photoinduced electron-hole pairs and how the energy released to obtain PL emission peak. PL is commonly utilized to evaluate the segregation and transfer performance of photogenerated charge carriers. Stronger peaks in PL analysis are therefore unfavorable for reducing rates of recombination. Contritely, reduced peak intensity is assumed to imply, reduce the rate of recombination, and higher charge separation efficiency and, as a result, more photocatalytic activity. The wavelength of photocatalysts has been proved to have a significant impact on PL spectral emission. The peaks have been obtained with visual wavelengths between 450 and 550 nm for all the photocatalysts [61]. For $V_2AlC$ MAX, there were PL intensities near to zero intensity because of its dark color, which reduced electron generation. When $V_2AlC$ was coupled with g-$C_3N_4$, the PL emission rate of $V_2AlC$ loaded g-$C_3N_4$ was obviously lowered. This implies that $V_2AlC$ can effectively inhibit photorecombination $e^-$ and $h^+$ again. Furthermore, the capacity of the $V_2AlC$ MAX phase to trap electrons in its ultrathin layered structure resulted in distinct optical and electronic properties that aided in the development of promising photocatalytic solar fuels. In comparison to $V_2AlC$ MAX, $V_2C$ MXene has relatively low PL emission peak, as seen in Fig. 3(a). This is most likely owing to MXene metallic composition, strong conductivity, and black color, and comparable findings have been found in the literature [61,62]. It is also worth mentioning that the photoluminescence of $V_2C$ nanosheets is excellent, owing to the creation of the direct energy band gap, which allows for radiative electronic transitions due to the reduction in system size [63]. The highest intensity peak in the PL spectrum of pure g-$C_3N_4$ was attributed to the band–band PL signal phenomenon, as illustrated in Fig. 3(b). The band–band PL signal is created by excitonic PL caused by n-$\pi$ * electronic transitions involving lone pairs of nitrogen atoms in g-$C_3N_4$, which results in a high rate of charge recombination. This demonstrates the presence of sub gap flaws in the g-$C_3N_4$ nanosheets, a phenomena that has been earlier observed [64]. More crucially, when compared to $V_2C$, $V_2AlC$, g-$C_3N_4$, and 10% $V_2AlC$/g-$C_3N_4$ samples, the charges separation proficiency in $V_2C$ loaded g-$C_3N_4$ composite sample was significantly greater. The $V_2C$/g-$C_3N_4$ composite illustrates the improvement in transfer of charge through the $V_2C$ and g-$C_3N_4$ nanosheets when the addition of $V_2C$ traps electrons, and results in the lowest PL intensity in the $V_2C$/g-$C_3N_4$ composite, signifying that the rate of recombination is decreased, facilitating charge transport over the interface between 2D $V_2C$ nanosheets and 2D g-$C_3N_4$ nanosheets. The composites with a loading of 15%$V_2C$ into g-$C_3N_4$ has the lowest excitation intensity due to the superior separation efficiency of photogenerated $e^-$-$h^+$ pairs generated by the interfaces between the two materials. More importantly, the fluorescent lifetime of the 15%

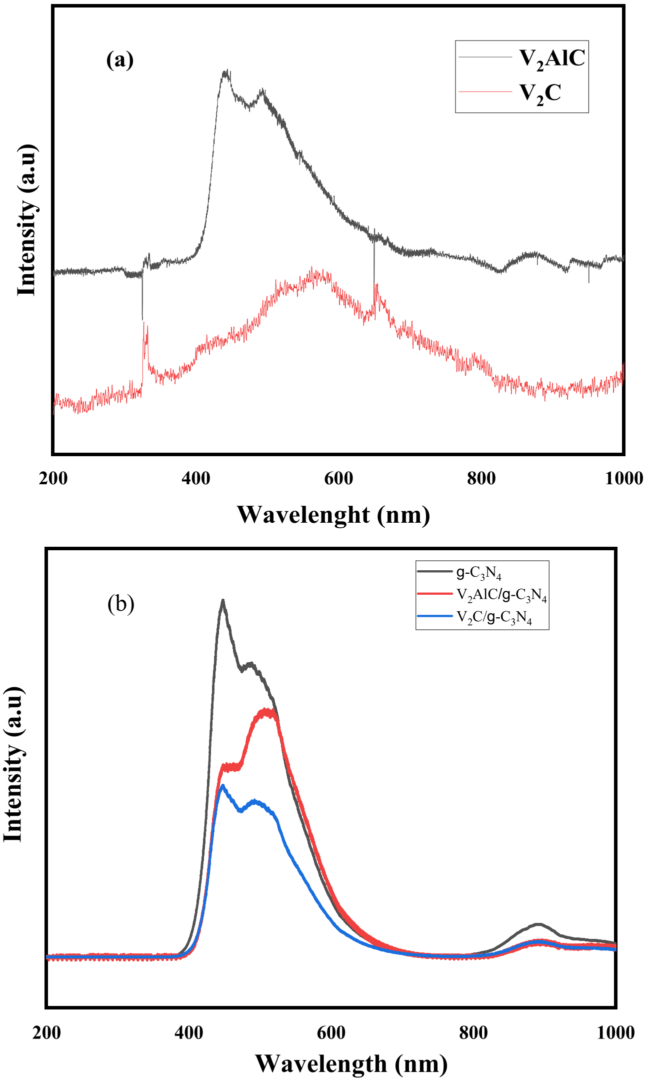

**Fig. 3.** (a) PL spectra of $V_2C$ an $V_2AlC$; (b) PL spectra of g-$C_3N_4$, 10%$V_2AlC$/g-$C_3N_4$ and 15%-$V_2C$/g-$C_3N_4$ samples.

$V_2C/g\text{-}C_3N_4$ sample is significantly shorter than that of $V_2AlC$, $g\text{-}C_3N_4$, $V_2AlC/g\text{-}C_3N_4$ sample, implying that an additional nonradioactive decay channel may be opened via electron transfer from 2D $g\text{-}C_3N_4$ nanosheets to 2D $V_2C$ MXene nanosheets due to the metal-like nature of $V_2C$, which can efficiently accelerate the separation of photogenerated charge carriers. This suggests that using $V_2C$ MXene as a mediator, the photogenerated recombination $e^-$-$h^+$ pairs in $g\text{-}C_3N_4$ can be effectively mitigated. As a result, a 2D/2D $V_2C/g\text{-}C_3N_4$ nanosheets with faster charge separation was successfully developed, which could be advantageous for boosting photocatalytic $CO_2$ conversion efficiency.

### 3.1.4. *Transient photocurrent response*

A variety of electrochemical tests were performed in order to study the separation of electron-hole pairs in the $V_2C/g\text{-}C_3N_4$ nanocomposite. The charge separation route in the heterostructure system was studied by measuring the EIS profiles of $V_2C$, $g\text{-}C_3N_4$, and 15 wt%– 48h$V_2C/g\text{-}C_3N_4$, and the results are shown in Fig. 4(a). The radius of each arc in EIS spectra was shown to be correlated with the efficiency of photogenerated carriers in the electrode/electrolyte interface layer resistance separation. Lower charge-transfer resistance may be achieved by reducing the arc radius, which in turn speeds up the separation of photogenerated carriers. Furthermore, on the EIS Nyquist plot, the arc radius of $V_2C$ is less than that of $g\text{-}C_3N_4$, and 15 wt%– 48h$V_2C/g\text{-}C_3N_4$, indicating that $V_2C$ MXene has a better charge carrier separation potential than pristine $g\text{-}C_3N_4$, and 15 wt% – 48 h $V_2C/g\text{-}C_3N_4$ nanocomposite. This is most likely owing to MXene metallic composition, which traps electrons and gives it a dark color, and similar observations have been reported in the literature [65]. The larger diameter of $g\text{-}C_3N_4$ indicates low electrical conductivity, which could prevent electron transmission. A smaller diameter of 15%-$V_2C/g\text{-}C_3N_4$ is detected compared to $g\text{-}C_3N_4$ and $V_2C$, showing that modified porous $g\text{-}C_3N_4$ designs can effectively boost the electrical conductivity of the polymer matrix and enable charge transfer towards photocatalytic redox reactions. More surprisingly, as shown in Fig. 4(a), the 15%-$V_2C/g\text{-}C_3N_4$ heterojunction has a lower radius than pristine $g\text{-}C_3N_4$. This means that when $V_2C$ MXene was added to pure $g\text{-}C_3N_4$, the efficiency of photogenerated carrier separation and the interfacial charge transfer potential of 15%-$V_2C/g\text{-}C_3N_4$ could be enhanced. These findings show that the development of this unique heterojunction, together with $V_2C$ MXene has high charge separation capacity, significantly enhances the efficiency of electron/hole pair separation and transfer within $V_2C/g\text{-}C_3N_4$ nanocomposite. As a result, 15%-$V_2C/g\text{-}C_3N_4$ heterojunction photocatalyst is expected to have significant photocatalytic activity when exposed to visible light, and this result corresponds to the PL measurement.

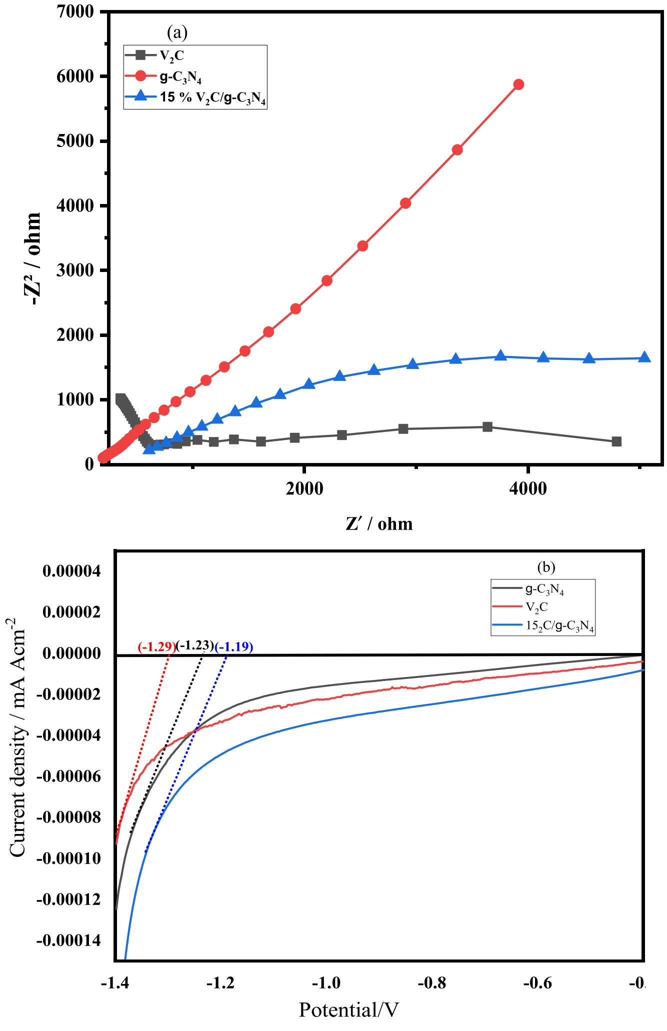

**Fig. 4.** (a) Pure $V_2C$ is plotted using EIS, pristine $g\text{-}C_3N_4$, and 15%– 48h$V_2C/g\text{-}C_3N_4$, (b) LSV of pure $V_2C$, pristine $g\text{-}C_3N_4$, and 15%– 48h$V_2C/g\text{-}C_3N_4$.

The photo responses of $V_2C$, $g\text{-}C_3N_4$, and 15%- $V_2C/g\text{-}C_3N_4$ were also investigated using linear sweep voltammetry under visible light irradiation, and the findings are given in Fig. 4(b). When the LSV curves of the three electrodes in 0.5 M KCl electrolyte are compared, similar outcomes have been obtained. The overpotential of the 15%– 48 h $V_2C/g\text{-}C_3N_4$ sample was (−1.19 V), which is less than the overpotentials of $g\text{-}C_3N_4$ (−1.23 V) and $V_2C$ (−1.29 V). In comparison to other electrodes, the (LSV) curve of a 15%– 48 h $V_2C/g\text{-}C_3N_4$ sample shows a dramatic transition from cathodic to anodic currents. As a result, this electrode has a higher charge collecting rate. Aside from the PL, and EIS data, this observation further supports the idea that loading $V_2C$ on $g\text{-}C_3N_4$ increases electron migration and would speed up the catalytic activity.

### 3.1.5. *Ultraviolet–visible (UV–Vis) spectroscopy*

The light absorption efficiency of photocatalyst is commonly evaluated by UV–vis DRS analysis, which is strongly related to photocatalytic performance. Therefore, the characteristics of the absorption optical of pure $g\text{-}C_3N_4$, pristine $V_2C$, and 15%-$V_2C$-$g\text{-}C_3N_4$ composites have been studied using UV–Vis diffuse reflectance spectroscopy (DRS) analysis. The $V_2C$ sample, as shown in Fig. 5(a), shows a broad absorption characteristic in the ultraviolet and visible ranges in the range 200–800 nm, which may be due to its dark color and metal-like nature [66]. Contritely, the spectrum of $g\text{-}C_3N_4$ exhibits a peak of absorption at 460 nm, which matches the absorption of observable light. There are many ways to modify and alter the band gap energy of graphitic carbon nitride, which is typically 2.70 eV, depending on the materials structure and surface treatment [67]. Clearly, prolonged stirring and subsequent sonication of $g\text{-}C_3N_4$ leads in an increased band gap toward visible light. The best optical absorption was produced by linking $V_2C$ to $g\text{-}C_3N_4$ in order to form a 2D/2D $V_2C/g\text{-}C_3N_4$ heterojunction. This is because the change is intrinsically linked to the synergistic effects of 2D $g\text{-}C_3N_4$ on the surface of 2D $V_2C$ nanosheets. The addition of 15%-$V_2C$ increased the wavelengths of adjusted $g\text{-}C_3N_4$ nanocomposite to better values in the visible light spectrum, with wavelengths of 468 nm as shown in Fig. 5(a). This also implies that the addition of $V_2C$ MXene can aid in the improvement of visible light harvesting, allowing for more efficient utilization of solar energy. This was most likely owing to increased development of $g\text{-}C_3N_4$ nanosheets, that resulted in increased absorption of light in the visible range. The Kubelka–Munk (K-M) function was used to calculate the band gap energies of $g\text{-}C_3N_4$ and 15%– 48 h $V_2C/g\text{-}C_3N_4$ materials according to Eq. (1), and the results shown in Fig. 5(a-c) [41].

$$E_g = (\alpha h\nu)^{\frac{1}{n}} \tag{1}$$

The tauc plot is a curve of converted $(\alpha h\nu)^{1/n}$ versus $h\nu$ from the data

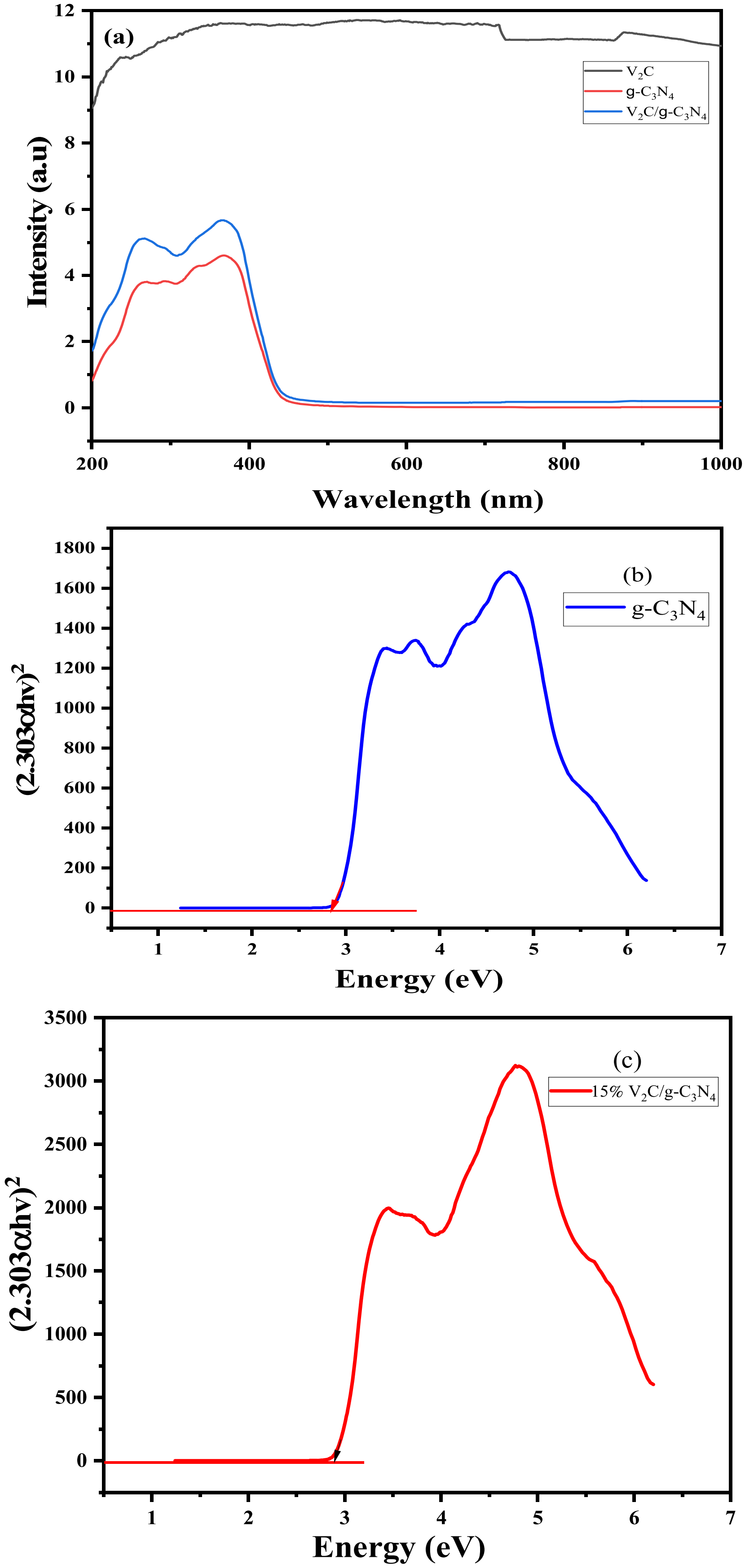

**Fig. 5.** (a) UV–vis spectrum of $V_2C$, g-$C_3N_4$, and 15% $V_2C$ /g-$C_3N_4$; (b) Tauc plot of g-$C_3N_4$, (c) Tauc plot 15% wt% $V_2C$ /g-$C_3N_4$.

of UV–vis spectra, where $E_g$, α, h and $\nu$ are energy band gap, absorption coefficient, Planck constant, and the frequency vibration, respectively. The value of n is well known to vary depending on the type of optical transition (n = 1/2 for direct transitions and n = 2 for indirect transitions). The value of n denotes the type of semiconductor used, which is selected to be 1/2 based on pure g-$C_3N_4$ material. The pure g-$C_3N_4$ and 15%-$V_2C$/g-$C_3N_4$ samples have band gap energies of 2.88 and 2.83 eV, respectively. It was demonstrated that by inserting $V_2C$, the g-$C_3N_4$ bang gap energy was somewhat altered, and the light absorption ability of 15%− 48 h $V_2C$/g-$C_3N_4$ in the visible range was boosted due to the dark color of $V_2C$. Band gap energy somewhat increased towards higher wavelengths due to g-$C_3N_4$ shading on the $V_2C$ surface and vanadium content in composite sample, which was clearly within visible light range. As a result, in the presence of $V_2C$, enhanced visible light absorption of 15%− 48 h $V_2C$/g-$C_3N_4$ composite would be helpful for boosting photocatalytic activity. The predicted g-$C_3N_4$ band gap energy was also used to calculate the locations of the valence band (VB) and conduction band (CB) using well-established empirical formulae as demonstrated in Eqs. (2) and (3) to better comprehend charge transfer routes and propose a mechanism with clear demonstration.

$$E_{CB} = X - E^e - 0.5E_g \tag{2}$$

$$E_{VB} = E_{CB} + E_g \tag{3}$$

The conduction and valance band edges are denoted by $E_{CB}$ and $E_{VB}$, respectively. χ is the geometric mean of a semiconductor's Mullikan electronegativity, which equals 4.73 eV in the case of g-$C_3N_4$, the hydrogen scale-free electron energy is referred to as $E^e$ and equal to (4.5 eV), and the g-$C_3N_4$ band gap energy is $E_g$ (2.88 eV). The conduction band of g-$C_3N_4$ was determined to be (−1.21 eV) using Eq. (2), whereas the valance band was determined to be 1.67 eV using Eq. (3). These results were consistent with previously stated VB and CB values of (1.67) and (−1.21) for pure g-$C_3N_4$, respectively [68]. All of these results demonstrate that the band gap energy of g-$C_3N_4$ can be changed by structural alteration and protonation. These findings also show the successful manufacture of a photocatalyst with good optical properties. This could be effective for promoting selective $CO_2$ conversion to fuels under visible light.

### 3.1.6. FESEM and EDX analysis

The surface morphology of $V_2AlC$, $V_2C$, g-$C_3N_4$, and 15%-$V_2C$/g-$C_3N_4$ nanocomposite have been illustrated in Fig. 6. The compact sheets structure of $V_2AlC$ is shown in Fig. 6(a). $V_2AlC$ is a dense layered structure composed of thick and compacted staked sheets with reduced interlayer spacing that are closely linked and packed together by a metallic bonding. $V_2C$ sheets with two-dimensional structure were formed after etching $V_2AlC$ MAX with HF for 48 h, as shown in Fig. 6(b-c). Additionally, $V_2C$ MXenes exhibit deformed and flexible MXene flakes, which could be a unique characteristic to increase the interaction between 2D $V_2C$ and other 2D materials [13]. These favorable structural characteristics suggest that $V_2C$ may be a potential candidate for flexible photocatalytic $CO_2$ reduction [45]. As illustrated in Fig. 6(d), g-$C_3N_4$ exhibits a characteristic nanosheet-like shape. This is because exfoliation of the g-$C_3N_4$ sheets that result in the 2D nanostructure. This demonstrates that melamine thermal processing using technique of ultrasonic has a noticeable impact on the formation of 2D nanostructures. The morphology of both two-dimensional $V_2C$ MXene, and g-$C_3N_4$ graphitic carbon nitride layers is illustrated in Fig. 6(e-f). Intriguingly, ultrasonic-assisted contact between g-$C_3N_4$ and $V_2C$ MXene has a clear effect on exfoliating nanosheets due to their good interaction with 2D $V_2C$ layers. The successful synthesis of conventional stacked 2D/2D heterojunction of $V_2C$ and g-$C_3N_4$ nanosheets was demonstrated in a 15%-$V_2C$/g-$C_3N_4$ sample. More crucially, in the composite sample, the g-$C_3N_4$ nanosheets growing on $V_2C$ nanosheets could be seen clearly. These results clearly demonstrate the feasibility of fabricating a 2D/2D heterojunction containing 15%− 48h$V_2C$/g-$C_3N_4$, which can increase the interfacial contact area for charge carrier migration. More electron transport routes are projected to be created as a result of the contact between $V_2C$ and g-$C_3N_4$, which is beneficial for electron transport and separation. As also shown in Fig. 7, an EDX mapping analysis was used to accurately investigate the distribution of elements in the composite sample. The EDX spectroscopy was performed on a 15%-$V_2C$/g-$C_3N_4$

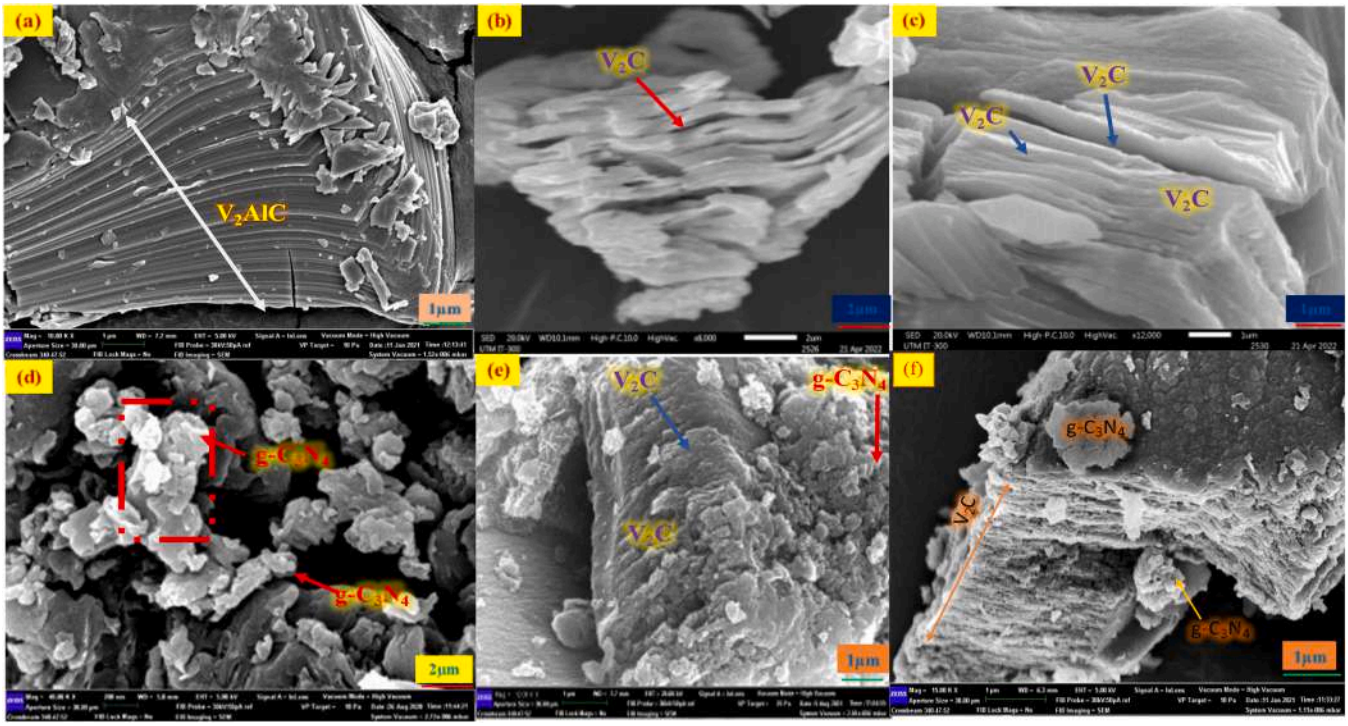

**Fig. 6.** $V_2AlC$ FESEM analysis, $V_2C$, g-$C_3N_4$, $V_2C$/g-$C_3N_4$ and their compounds: (a) SEM image of $V_2AlC$, (b-c) SEM images of $V_2C$, (d) SEM image of g-$C_3N_4$, (e-f) SEM images of $V_2C$/g-$C_3N_4$ at different magnification.

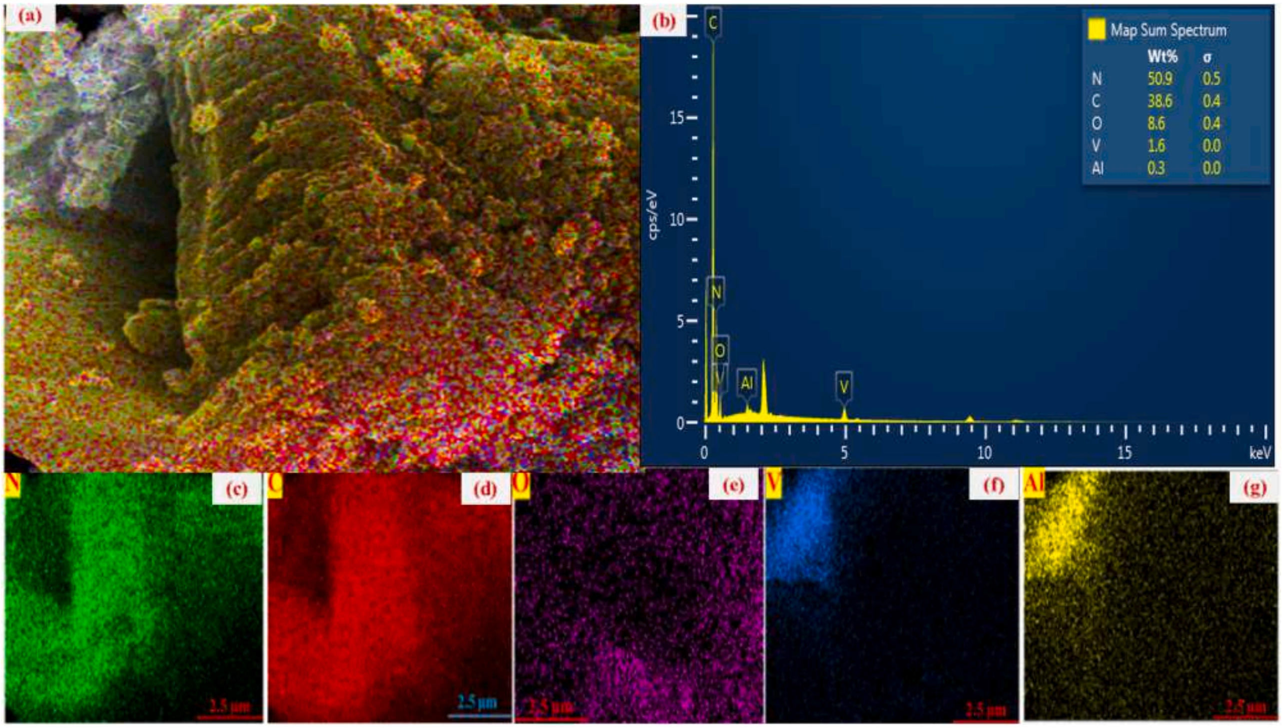

**Fig. 7.** EDX measurement of a 15%-$V_2C/g-C_3N_4$ catalyst material; (a) SEM showing mapping distribution, (b) EDX plots of the nanocomposite.

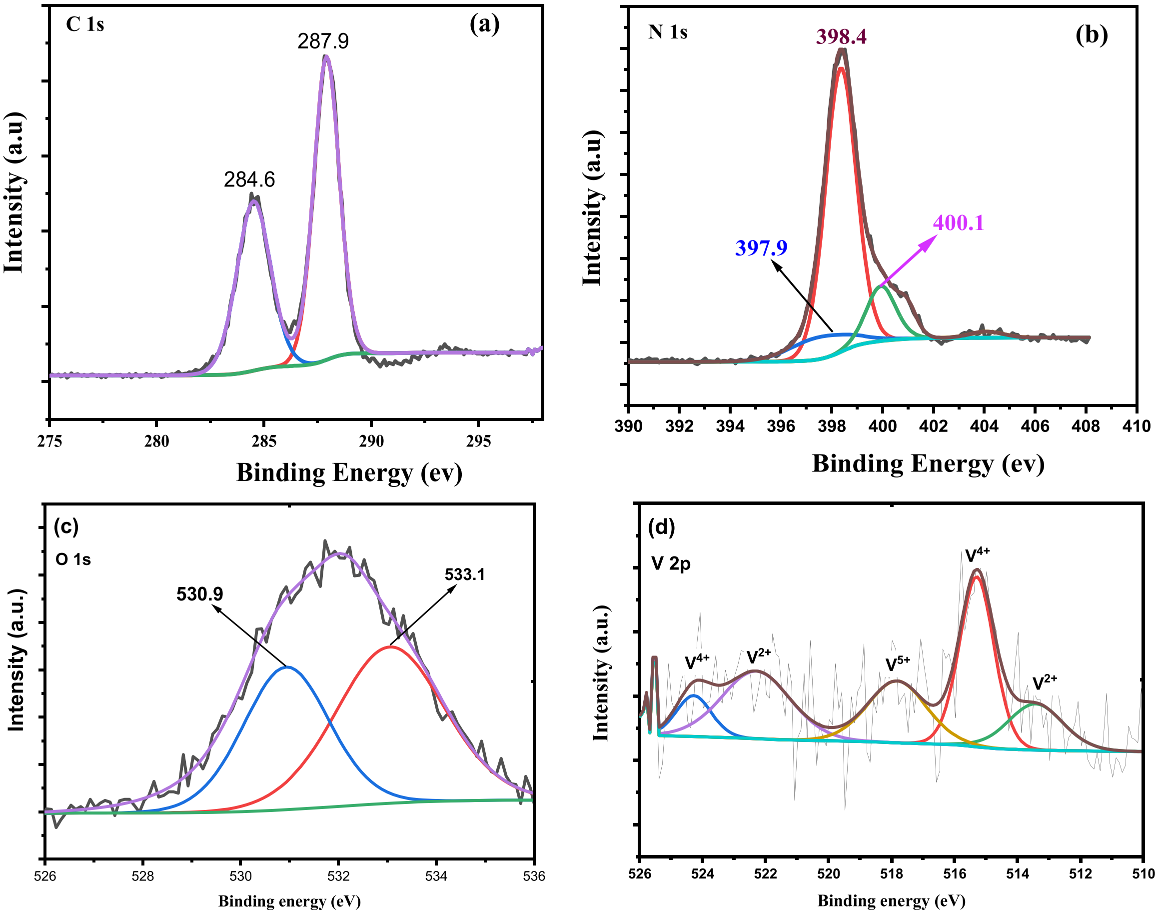

**Fig. 8.** High resolution XPS spectra of $V_2C/g-C_3N_4$ (a) C 1s, (b) N 1s, (c) O 1s and (d) V 2p.

composite in order to guarantee that the $V_2C$ dispersion in the composite was consistent. Fig. 7(a) depicts the consistent distribution of elements over the composite catalyst. Fig. 7(a) shows also the good interaction and homogeneous distribution of elements in the $V_2C$ and g- $C_3N_4$ nanosheets in the EDX layered image. The presence of all elements in the composite catalyst is further confirmed by the EDX data in Fig. 7(b). The existence of the main constituents of the $V_2C$-g-$C_3N_4$ nanocomposite is supported by the elemental analysis in the EDX mapping image. These elements include nitrogen, carbon, oxygen, vanadium, and Aluminum with elemental atomic ratios of 50.9%, 38.6%, 8.6%, 1.6% and 0.3%, respectively. However, as seen in Fig. 7, a denser green, blue, and red color on the right shows that the sample includes more nitrogen, carbon, and oxygen, which is mostly due to the existence of g-$C_3N_4$. Finally, the nanocomposite was synthesized with a high degree of purity due to the presence of prediction elements in $V_2C$-g-$C_3N_4$ photocatalysts.

### 3.1.7. *XPS analysis*

The elemental states of the of 15%-$V_2C$/g-$C_3N_4$ composite was examined utilizing X-ray photoelectron spectroscopy (XPS), as shown in Fig. 8. Fig. 8(a) shows C 1 s XPS spectrum with two significant peaks having binding energies at 284.6 and 287.9 eV corresponding to C-C and N-C═N. Fig. 8(b) shows N 1 s spectrum for the compounds with binding energies 397.9, 398.4, and 400.1 eV, which are assigned to pyridine-N ($sp^2$-bonded nitrogen) in the triazine ring (C-N═C), ternary nitrogen (N-$C_3$), and the amino group (C-N-H), respectively [65]. The O 1 s XPS spectrum in Fig. 8(c) shows two peaks with binding energies 530.9 and 533.1 eV attributable to presence of oxygen vacancies and presence of hydroxyl group. As illustrated in Fig. 8, (d), spectrum of V 2p can be fitted with three peaks at 513.5, 515.4, and 517.8 eV, corresponds to $V^{2+}$, $V^{3+}$ and $V^{5+}$ with their doublets at 522.3 and 524.4 eV, respectively [69].

These XPS analysis results were compared to those of analogous studies that have previously been reported in the literature utilizing pure g-$C_3N_4$ and pure $V_2C$, respectively. Previously, we studied the XPS analysis of pure g-$C_3N_4$ and found that the binding energies were almost the same compared to the result of this study, thereby verifying the successful production of g-$C_3N_4$ in 2D/2D g-$C_3N_4$/$V_2C$ composite without any band shift. The $sp^2$ hybridized carbon (NC═N) and C-C are responsible for the spectrum at 288.45 and 284.85 eV, while the N 1 s, the peak at 398.68, 400.74, and 401.18 eV, are due to the bicoordinated ($N_2C$) and tricoordinated ($N_3C$) nitrogen atoms and N-$H_x$ groups in the heptazine structure of g-$C_3N_4$. Likewise, For Pure $V_2C$ MXene, the results were almost in good agreement with $V_2C$/g-$C_3N_4$ composite. In the $V_2C$, V, C and O elements were found. The presence of O could be attributable to the slight surface oxidation of $V_2C$ that occurred during the preparation process. [70]. Briefly, the XPS results reveal that a 2D/2D $V_2C$/g-$C_3N_4$ nanocomposite was successfully synthesized when compared to the XPS results of pure g-$C_3N_4$ and pure $V_2C$ MXene, respectively, which were obtained from the previous literature.

## 3.2. *Photocatalytic $CO_2$ reduction with $H_2O$*

Prior to starting the actual experiments, several initial experiments were performed under identical experimental conditions to ensure that each and every product produced was generated solely from $CO_2$ as a consequence of the photocatalysis process. To initially verify whether or not products such as CO and $CH_4$ were generated, quality control tests were performed utilizing photocatalysts and light without reactants, whereas another experiment was conducted without photocatalyst in the presence of a feed mixture under light irradiation. Both products (CO and $CH_4$) were observed to be formed not from the photocatalyst individually or from any other resources, but as a consequence of carbon dioxide reduction during a photocatalytic activity process utilizing light irradiation and photocatalyst. The quality control experiments confirmed that the photocatalysts is clean and that carbon-based products such as CO and $CH_4$ were generated during the photocatalytic $CO_2$ reduction process.

### 3.2.1. *Performance comparison between $V_2AlC$ MAX and $V_2C$ MXene*

The MXene sheets originating from Al-containing MAX phases can be synthesized using hydrofluoric acid (HF) as an etching solution. Diverse MXenes layered can be constructed by acid etching (HF etching) at room temperature by regulating the concentration of HF and reaction time [71]. When MAX phases are exfoliated into 2D MXenes nanosheets, the transition metals, thickness, and surface functionality exhibit quite different electronic, magnetic, optical, and electrochemical properties that are rarely seen in their original MAX phases. This will have a different effect on the bulk material and alter its properties. It is also revealed that the terminal groups of the nanosheets can be varied using different exfoliants solution during the fabrication processes [72]. All these factors can be used to optimize MXenes properties for the applications in photocatalytic $CO_2$ reduction. The results presented here provide fundamental insights on MAX and MXene phases and can be used to obtain a more complete picture of MAX and MXene to couple with another photocatalyst to determine the efficiency of both of them to improve the generation of CO and $CH_4$ during photocatalytic $CO_2$ conversion.

To investigate the effect of 2D $V_2AlC$ MAX and 2D $V_2C$ MXene on the photocatalytic activity of g-$C_3N_4$ for photocatalytic $CO_2$ reduction with $H_2O$, several samples were synthesized including 2D $V_2AlC$ MAX/g-$C_3N_4$ and 2D $V_2C$ MXene/g-$C_3N_4$ composites. When $V_2AlC$ was coupled with g-$C_3N_4$ to form $V_2AlC$/g-$C_3N_4$, different $V_2AlC$ MAX amounts of 5%, 10%, and 15% were loaded onto the pure g-$C_3N_4$ sample, as illustrated in Fig. 9. The rates of generation of both products increased steadily with the addition of $V_2AlC$ up to 10% wt. Optimal CO and $CH_4$ production was found to be 134 and 185 μmol $g^{-1}$ after 4 h with 10% $V_2AlC$ loaded over g-$C_3N_4$, which is 6.1 and, ~1.2 times greater than what was produced over g-$C_3N_4$, respectively. This could be interpreted in terms of the availability of irradiation active sites, with boosting the catalyst loading providing additional active sites for the reaction. Nevertheless, increasing the $V_2AlC$ loading onto g-$C_3N_4$ by 15 wt% leads in a drop of CO (129 μmol $g^{-1}$) and $CH_4$ (179 μmol $g^{-1}$) values. This decreased could be ascribed to a variety of factors; for example, the excessive $V_2AlC$ contents effectively covers the active sites on the g-$C_3N_4$ surface, or at the very least reduces their availability, thereby decreasing the overall photocatalytic activity, as the $CO_2$ reduction process happens on the surface of g-$C_3N_4$. More importantly, the bulk structure of $V_2AlC$ is provided by compact sheets, thereby g-$C_3N_4$ can only be spread partially the bulk surface, resulting in poor interfacial interactions between the two materials. Although, coupling $V_2AlC$ is beneficial for transporting electrons, however, an excess quantity should have adverse effects on the photocatalytic performance for $CO_2$ reduction.

Relatively, compared to $V_2AlC$ MAX, 2D $V_2C$ MXene was shown to be more effective for charge carrier transport and segregation. Fig. 10 (a-b) illustrates the influence of $V_2C$ MXene loading on the photocatalytic efficiency of g-$C_3N_4$ for $CO_2$ reduction with $H_2O$ during CO and $CH_4$ generation. Different $V_2C$ MXene contents of 5, 10, 15 and 20 wt% have been presented to the pristine g-$C_3N_4$ sample. CO and $CH_4$ are found as the primary products when all types of photocatalysts are used, with $CH_4$ production being the highest. Moreover, the $V_2C$ introduction has a considerable effect on photocatalytic CO and $CH_4$ generation, which increased as the $V_2C$ MXene amount increased, reaching up to 15% for CO and $CH_4$, respectively. As the $V_2C$- loading grows from 15 to 20 wt%, the CO and $CH_4$ production gradually decline. The generation of $CH_4$ increased constantly with the irradiation period for all samples tested, as shown in Fig. 10 (a). It can be clearly seen that optimized amount of $V_2C$ loading is 15 wt%, where 15 wt%$V_2C$/g-$C_3N_4$ exhibits highest photoactivity for the production of $CH_4$ with yield rates 205 μmole $g^{-1}$, which is 6.7, and 1.1 folds higher compared to g-$C_3N_4$ and 10% $V_2AlC$/g-$C_3N_4$ samples, respectively. Similarly, highest CO production over 15%$V_2C$/g-$C_3N_4$ of 151 μmole $g^{-1}$ was achieved, which is ~1.3, and 1.1 times higher compared to g-$C_3N_4$ and 10% $V_2AlC$/g-$C_3N_4$ samples, as shown

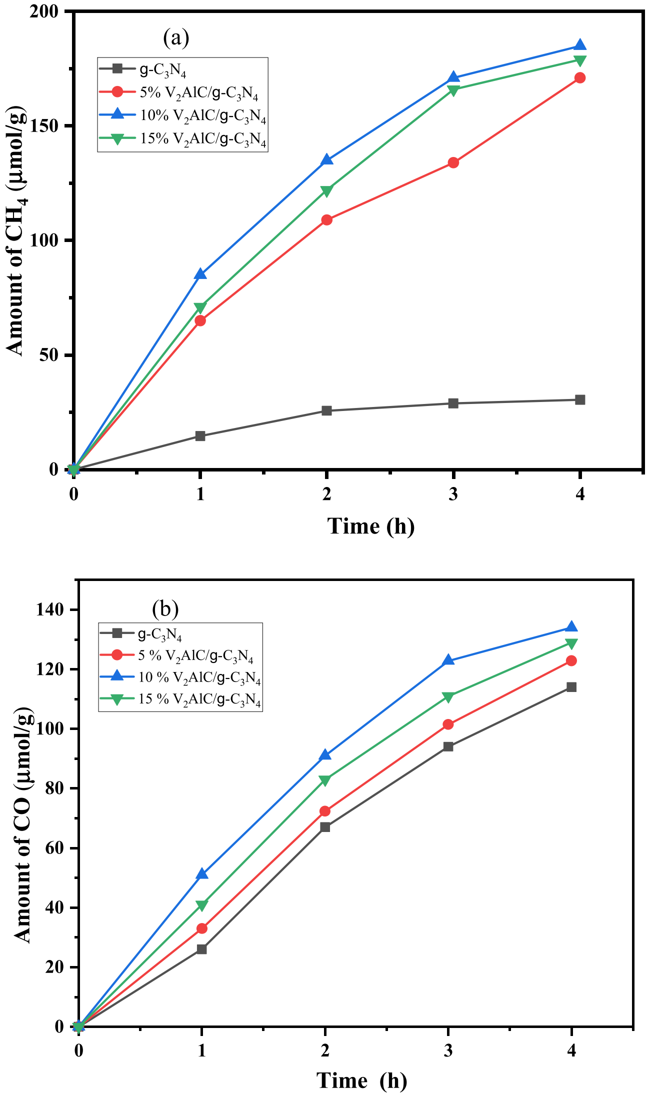

**Fig. 9.** Performance analysis of g-$C_3N_4$, $V_2AlC$/g-$C_3N_4$ for the generation of CO and $CH_4$ via photocatalytic $CO_2$ conversion under visible light: (a) $CH_4$ generation, (b) CO generation.

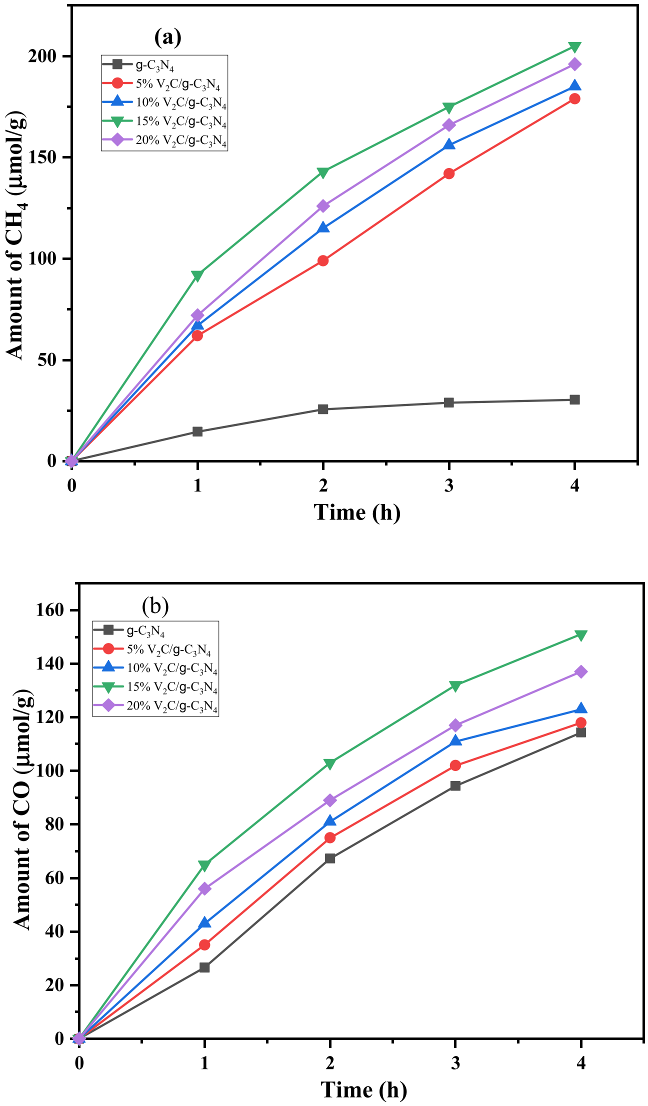

**Fig. 10.** Analysis of g-$C_3N_4$ and $V_2C$/g-$C_3N_4$ performance for the generation of CO and $CH_4$ via photocatalytic $CO_2$ reduction under visible light: (a) $CH_4$ generation, (b) CO generation.

Fig. 10 (b), respectively. It can be also clearly seen that the efficiency of $V_2C$-loading is much noticeable for $CH_4$ generation than CO. This significantly improved activity with the loading of $V_2C$ into g-$C_3N_4$ was due to its conductive properties and working as a mediator for transporting charge carrier [73]. These observations revealed that $V_2C$-loading to the pure catalyst (g-$C_3N_4$) makes it very efficient for $CH_4$ production. However, a decreased in CO, and $CH_4$ production rate per unit mass were observed with increasing catalyst loading, this behavior has been observed in a number of other investigations [20,74]. The formation of charge recombination centers over the g-$C_3N_4$ surface is likely to be the cause of the reduction in photoactivity at increased $V_2C$ loading. As a result, the quantity of $V_2C$ MXene in the g-$C_3N_4$ structure influences the photocatalytic efficiency of the photocatalyst.

The results presented here provide comprehensive comparison on MAX and MXene phases and can be used to obtain a more complete picture of MAX and MXene to couple with another photocatalyst to determine the efficiency of both of them to improve the production rate of CO and $CH_4$ during photocatalytic $CO_2$ reduction. The $CH_4$ production rate over the heterostructure 2D/2D $V_2AlC$/g-$C_3N_4$ and 2D/2D $V_2C$/g-$C_3N_4$ composite was highest than the single g-$C_3N_4$ semiconductor. Heterojunction semiconductors are an effective method for electron-hole separation to decrease energy-wasting electron-hole recombination, in contrast to single photocatalysts. This is owing to the increased production of electrons and protons, effective visible light absorption, rapid charge transfer and inhibited recombination rate, porous structure, and appropriate oxidation potential, an abundance of active sites, huge specific surface area, which results in selective methane production [17]. The increased activity was caused by using cocatalyst such as $V_2C$ MXene and $V_2AlC$ MAX phase, which has excellent electrical conductivities and significant $CO_2$ adsorption capabilities. Due to the synergistic effects of g-$C_3N_4$ and $V_2C$ in preventing charge recombination and providing multiple electron separation routes for the conversion of $CO_2$ to $CH_4$., Thus, he 2D/2D $V_2C$/g-$C_3N_4$ composite catalyst produced the most methane.

These results could be elucidated based on rate of production of CO and $CH_4$ for g-$C_3N_4$, 10%$V_2AlC$/g-$C_3N_4$, and 15%-$V_2C$/g-$C_3N_4$ samples as shown in Fig. 11. To begin with, the existence of Al in the MAX structure makes $V_2AlC$ lower conductive than $V_2C$ MXene. As a result, the separation of charges in $V_2AlC$/g-$C_3N_4$ would be less effective than in $V_2C$/g-$C_3N_4$ heterojunction. Second, compared to $V_2C$/g-$C_3N_4$, the contact between $V_2AlC$/g-$C_3N_4$ is poor, since MXene nanosheets have a higher conductivity than bulk material [72]. Additionally, the expectation that high electrical conductivity and the hydrophilic nature will

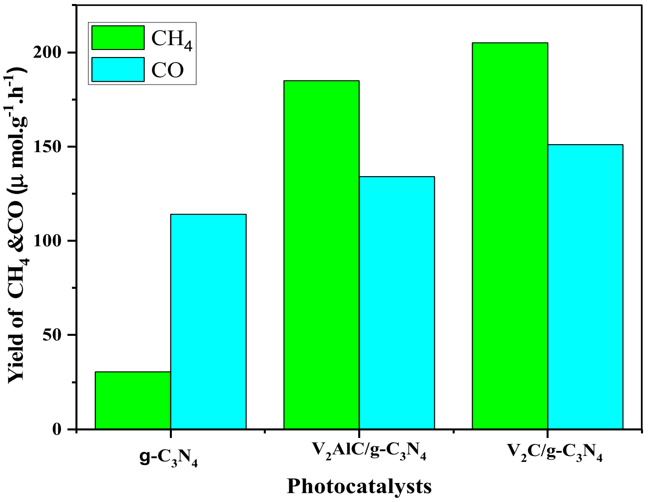

**Fig. 11.** Performance analysis of g-$C_3N_4$, 10% $V_2AlC$/g-$C_3N_4$, and 15%$V_2C$/g-$C_3N_4$ for the generation of $CH_4$ and CO via photocatalytic $CO_2$ reduction under visible light.

accelerate an electrochemical reduction of $CO_2$, in consideration of both giving electrons and $H^+$ attachment [71]. More importantly, because $V_2AlC$ is made up of compressed sheets that provide bulk structure to $V_2AlC$, and because g-$C_3N_4$ can only be spread over the bulk surface, thereby there is poor interaction between the two materials. Furthermore, charges generated over the g-$C_3N_4$ have a greater possibility for the rate of recombination than charges transferred to $V_2AlC$, leading to decrease activity throughout the $CO_2$ reduction process. In contrast, the $V_2C$ layer structure has been exfoliated, whilst the single-layered structure of g-$C_3N_4$ has been intimately intertwined. Therefore, a two-dimensional heterojunction is beneficial to promote photoactivity due to excellent charge carrier separation properties [75]. Photo-generated electrons could be efficiently segregated from the g-$C_3N_4$ surface during visible light irradiation, leading to increased $CO_2$ conversion to methane. Thus, enhanced performance of g-$C_3N_4$ loaded with $V_2C$ was due to 2D/2D heterojunction formation and synergistic effects between $V_2C$/g-$C_3N_4$, which results efficient photo-generated charges separation for selective photocatalytic $CO_2$ conversion to fuels. Therefore, the conductive properties of $V_2AlC$ MAX phase and $V_2C$ MXene nanosheets and their interfacial interface with g-$C_3N_4$ to form an excellent heterojunction is the most important factors to enhance photocatalysis activity. Previously, reduction of $CO_2$ by photocatalysis over a 2D/2D/2D O-$C_3N_4$/Bt/$Ti_3C_2T_x$ nanocomposite to CO has been studied utilizing visible light [48]. It enabled a more intimate interface engagement with higher efficiency of photocatalysis. Another confirmation of how materials combine to promote photocatalytic activity and so enhances $CO_2$ reduction is provided by this study [20].

### 3.2.2. *Effect of different catalyst loading*

Solar fuel production efficiency at varied catalyst loadings under visible light irradiation using 15%-$V_2C$/g-$C_3N_4$ is depicted in Fig. 12. Fig. 12 (a) shows the irradiation time required to produce $CH_4$ at various photocatalyst loadings ranging from 25 to 150 mg. The best $CH_4$ evolution was observed with a photocatalyst loading of 50 mg. $CH_4$ generation per unit mass was increased when the 15%-$V_2C$/g-$C_3N_4$ catalyst loading was raised from 25 to 50 mg. However, as the photocatalyst loading was increased from 50 to 100 and 150 mg, it began to drop, and the trends were consistent throughout the reaction. The $CH_4$ production was 1.2, ~1.1, and 1.3 times greater at 50 mg than at 25, 100, and 150 mg, respectively. This enhanced rate of production was attributed to the use of an appropriate catalyst loading and the presence of a larger active surface for initiating photocatalytic $CO_2$ reduction. Contritely, the decreased in $CH_4$ formation was attributed to less available surface area exposed to light irradiation. More importantly, better light absorption and increased catalyst sensitivity for $CO_2$ reduction light irradiation absorption were obviously responsible for this enhancement. All of the findings indicate that exposing the active sites on the surface of the photocatalyst to adequate light irradiation could alter and enhance the photocatalytic $CO_2$ reduction process.

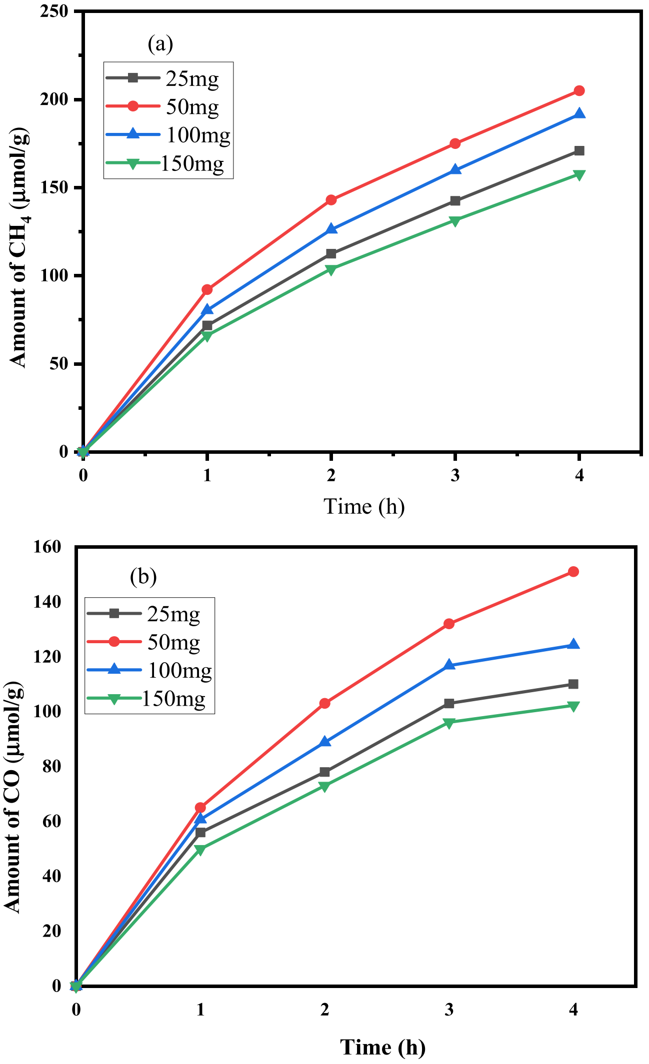

**Fig. 12.** The impact of varied catalyst loadings (15 wt% $V_2C$/g-$C_3N_4$) on photocatalytic $CO_2$ conversion to CO and $CH_4$ under visible light; (a) $CH_4$ generation, (b) CO generation.

Fig. 12(b) shows that CO generation trends are quite similar to those of $CH_4$, with a maximum yield of 50 mg of catalytic loading. At higher catalyst loadings, such as 100 mg and 150 mg, as well as at the lowest catalyst loading of 25 mg, photoactivity for CO and $CH_4$ generation was shown to be inefficient. The CO production rate was 1.3, ~1.1, and 1.3 times higher with catalyst loading of 50 mg, respectively. As a result of increased or lower catalyst loading, the CO development rate per unit mass will be lowered. This was most likely owing to the photochemical reaction having a smaller exposed catalyst surface accessible. Furthermore, the amount of light irradiated on the catalyst surface determines the production rates. All of these findings indicated that additional catalyst loading has an effect on CO and $CH_4$ production, whereas, the generation rates per unit mass were attained as an outcome of the decreased photocatalyst loading. However, in some circumstances, the generation rate can be increased while retaining the same reaction conditions by increasing catalyst loading [14]. These results indicate that optimized catalyst loading is crucial to obtaining improved production and selectivity when using solar energy.

### *3.2.3. Effect of pressure*

The photocatalysis performance of a 15%-$V_2C$/g-$C_3N_4$ composite was tested at three different $CO_2$ gas pressures (0.3, 0.4, and 0.6 bars). Both $CH_4$ and CO generation rates were enhanced with increasing pressure, reaching up to 266.5 and 172.9 μmol $g^{-1}$ at 0.4 bar, respectively, as shown in Fig. 13 (a-b). This is due to a variety of factors, including the following: (i) Pressure rises $CO_2$ concentration and availability on the photocatalyst surface, (ii) More $CO_2$ and water molecules collide with photogenerated $e^-$-$h^+$ pairs in a narrow region when the reactor pressure rises which increases the rate of photoreaction, (iii) By reducing the boundary layer thickness and raising pressure, photocatalyst nanosheet boundary layers are able to transfer mass more quickly, (iv) With increasing pressure, $CO_2$ gas adsorption and diffusion rates through the photocatalyst pore mouth increases [76,77]. This can happen as a result of $CO_2$ molecules competing for adsorption on the binary composite active sites during the photocatalytic reduction process. However, as the pressure was increased from 0.4 to 0.6 bar, the CO and $CH_4$ production began to drop, and the trend was maintained throughout the reaction. The influence of rising $CO_2$ pressure on photocatalytic conversion to $CH_4$ with a $TiO_2$ photocatalyst was also investigated by Kaneco and colleagues [78]. The findings suggest that the production of methane begins to decline at pressures greater than 2.8 MPa. Tseng et al. [79] stated that the $CH_3OH$ produce increased greatly as $CO_2$ pressure was increased up to 125 kPa and then began to drop.

### *3.2.4. Effect of reforming systems*

Further investigation of the efficiency of a 15%-$V_2C$/g-$C_3N_4$ heterojunction was conducted using various $CO_2$ reducing agents. As the reductants, $CO_2$ reduction experiments were carried out using water ($CO_2$ +$H_2O$), hydrogen ($CO_2$ +$H_2$), and a methanol–water mixture ($CO_2$ + 10% $CH_3OH$), respectively. The CO and $CH_4$ were the primary $CO_2$ reduction products in all of the experiments. The $CH_4$ production was increased when methanol was added to water as sacrificial reagent, as shown in Fig. 14 (a). The maximum methane evolution rate of 254 μmol $g^{-1}$ was attained using a methanol–water mixture ($CO_2$ + 10% $CH_3OH$), which is approximately 1.2 and 1.6 times greater than that achieved using water ($CO_2$ +$H_2O$) and hydrogen ($CO_2$ +$H_2$) photocatalytic systems, respectively. This is because when methanol was added to the feed mixture, the rate of $CH_4$ generation increased, owing to the increased production of protons ($H^+$) as demonstrated in Eqs. (4) and (5). Accordingly, the presence of a proton-rich reaction system would be ideal for the production of $CH_4$.

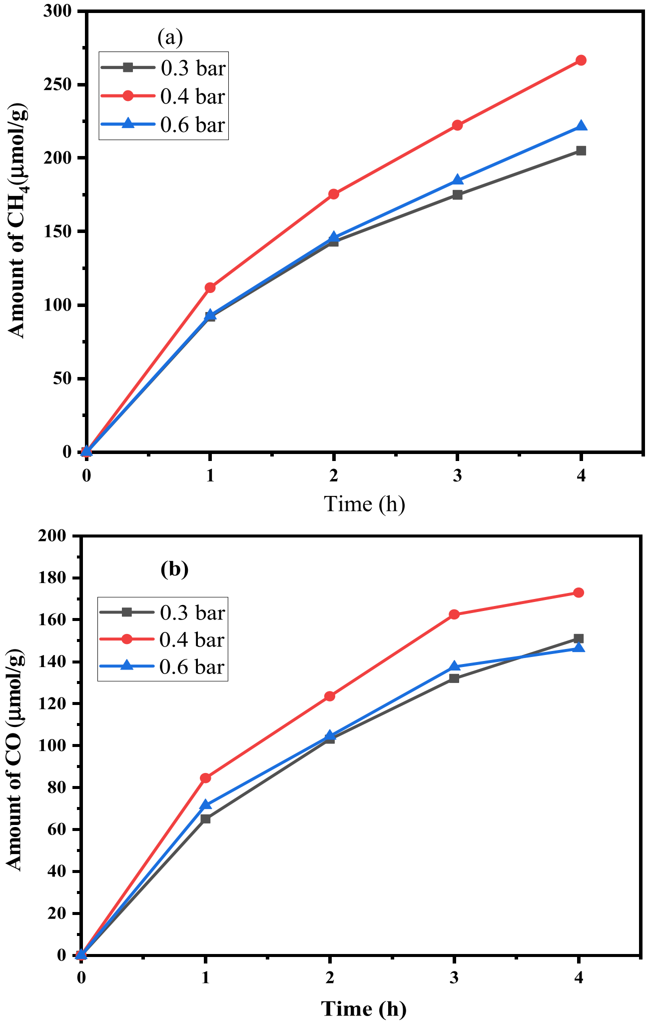

**Fig. 13.** The effect of varied pressure values (0.3, 0.4, and 0.6 bar) on the efficiency of a $V_2C$/g-$C_3N_4$ nanocomposite for photocatalytic $CO_2$ reduction to CO and $CH_4$ in visible light: (a) CO generation, (b) $CH_4$ generation.

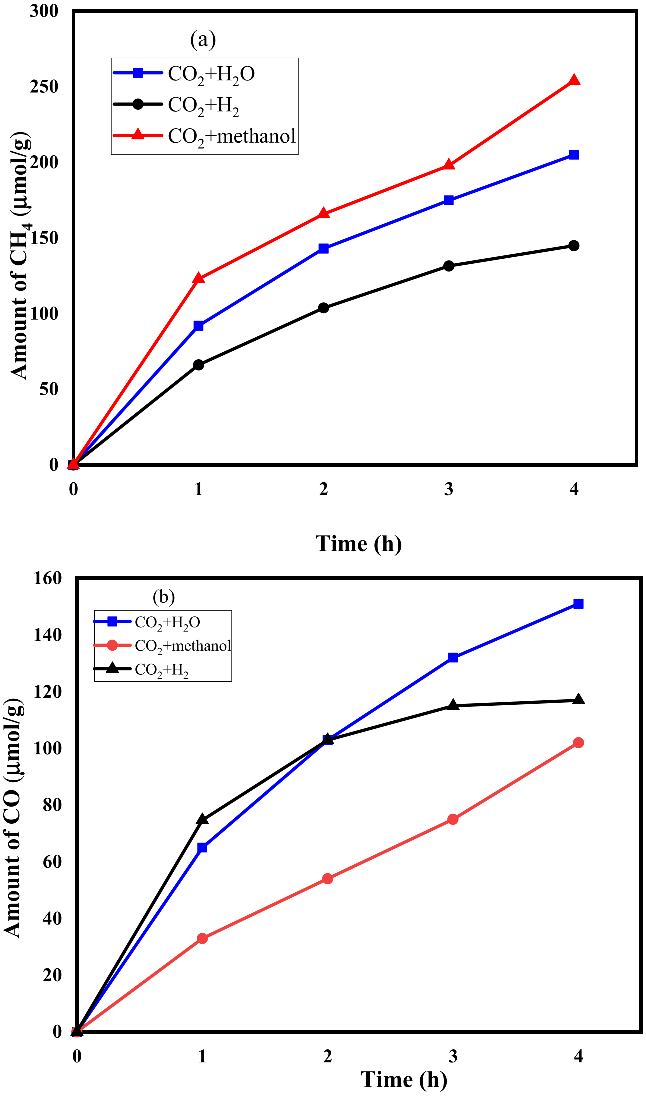

**Fig. 14.** (a) The impact of a reducing agent on the efficiency of a 15%-$V_2C$/g-$C_3N_4$ for $CH_4$ evolution, (b) Performance of 15%-$V_2C$/g-$C_3N_4$ nanocomposite for CO using several reducing agents.

$$CH_3OH + H_2O \rightarrow CO_2 + 3H_2 \quad (4)$$

$$CH_3OH \rightarrow CO + 2H_2 \quad (5)$$

Thus, the use of sacrificial reagents (10 vol% methanol-water mixture) could improve photocatalytic $CO_2$ reduction process. The sacrificial reagents not only promote higher proton production but also contribute to providing electrons throughout the oxidation process, resulting in increased $CH_4$ formation. Enhanced $CH_4$ yield using methanol-water combination over the composite catalyst can help increase numerous parameters such as electron transfer rate, hole scavenger contribution, proton generation and efficient feed mixture adsorption in a methanol nature of feed mixture and photocatalyst [80]. Earlier, we examined photocatalytic $CO_2$ conversion over a $Ti_3AlC_2$/g-$C_3N_4$/$TiO_2$ composite in the presence of methanol as a sacrificial reagent, and hydrogen was produced as the primary product during the irradiation [81]. All of these results demonstrate that sacrificial reagents contribute greatly to $CH_4$ generation by limiting charge carrier recombination and by delivering additional protons via photo-reformation. These findings support the utilize of $CH_3OH$ as a potential sacrifice reagent and 15%-$V_2C$/g-$C_3N_4$ as an effective composite catalyst for photocatalytic $CO_2$ reduction to $CH_4$ under light irradiation.

As illustrated in Fig. 14 (b), a large amount of CO was noticed at the beginning of the chemical process when a $CO_2$-water system was used. This amount increases with the reaction time. After 4 h of irradiation, the greatest CO generation was achieved utilizing the $CO_2$-water system, followed by the $CO_2$ + 10% $CH_3OH$ mixture and hydrogen $CO_2$ +$H_2$ photocatalysts system. The production of CO in $CO_2$-$H_2O$ reaction system is depicted in Eq. (6). The highest CO development rate of 151 μmolg$^{-1}$ was obtained by the $CO_2$-water system, which is evidently 1.4 and 1.2 times greater than that obtained using the $CO_2$-methanol–water and $CO_2$-$H_2$ photocatalytic systems, respectively. However, the production of CO is still lower than $CH_4$ production over 15%-$V_2C$/g-$C_3N_4$ nano catalysts. This is due to the lower photon energy requirement in $CO_2$ reduction utilizing $H_2O$ reductant and the lower adsorption of $CO_2$ and $H_2O$ over the catalyst surface [82]. Furthermore, $CO_2$ would adsorption less effectively over 15% -$V_2C$/g-$C_3N_4$ catalyst due to the basic character of the catalyst, resulting in decrease CO yield. This could be also explained by differences in $H_2O$ adsorption on the catalyst surface. However, $H_2O$ aided $CO_2$ conversion, resulting in an adequate amount of CO being produced [32]. It appears that appreciable amounts of CO and $CH_4$ were produced during $CO_2$ reduction with $H_2$ as reducing agent. This also confirms that any hydrogen produced during the water oxidation process is consumed by $CO_2$ in the production of CO and $CH_4$. However, during $CO_2$ reduction with hydrogen, production of CO and $CH_4$ were the lowest compared to water ($CO_2$ +$H_2O$), and a methanol-water mixture ($CO_2$ +10% $CH_3OH$), respectively Previously, Xiong and colleagues detailed the possible CO and $CH_4$ production during $CO_2$ reduction with water as reducing agent. Our team studied the impacts of $H_2O$/$H_2$ on the efficiency of a $WO_3$/g-$C_3N_4$ nanocomposite in another work and observed that when $H_2$ was utilized as the reducing agent, CO generation increased [14].

$$2CO_2 + 3H_2O \xrightarrow{light,Cata} CH_4 + CO + H_2 + 2O_2 \quad (6)$$

### 3.3. Stability analysis

A critical aspect of photocatalytic $CO_2$ reduction systems is the investigation of the catalyst lifetime, which also known as the stability of the photocatalyst, when it is used in a variety of applications, as shown in Fig. 15. The stability of the 15%-$V_2C$/g-$C_3N_4$ composite was evaluated in cyclic runs to ensure that CO and $CH_4$ production continues throughout $CO_2$ photoreduction under similar conditions. Three consecutive cycles of 12 h each were used to perform the stability analysis. To accomplish this, a fixed-bed photoreactor was used, and 50 mg of photocatalyst has been placed into the photoreactor. After each cycle, the procedure was repeated until the 3rd cycle, where the results for the constant evolution of $CH_4$ and CO could be seen in Fig. 15. However, it was observed that after the third cycle, the rate of CO and $CH_4$ evolution decreased by a small amount. After the first cyclic cycle, many studies report that photocatalysts deactivate with a negligible reduction in photocatalytic CO2 reduction [83]. A variety of factors can cause catalysts to lose their photoactivity, including the presence of oxygen in the solution, intermediate products blocking catalyst sites, morphological changes in response to light irradiation, and carbon production during chemical reactions [81]. The optimum $CH_4$ and CO of 205 and 151 μmol g$^{-1}$ were attained after the first cycle, respectively. However, the amount of CO and $CH_4$ produced is still adequate after the third cycle, which was 46.4 and 129.3 mol g-cat$^{-1}$, albeit lower than the amounts produced in the first and second cycles. Although, the photocatalysts efficiency has been reduced by multiple cycles, the production

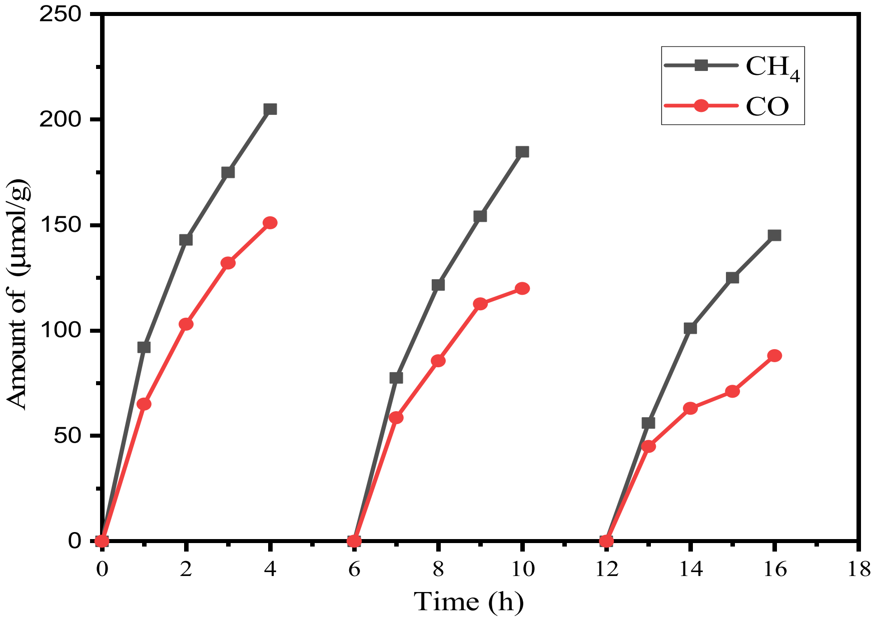

**Fig. 15.** The photocatalytic $CO_2$ reduction stability analysis of 15%-$V_2C$/g-$C_3N_4$ with production of CO and $CH_4$ under visible light.

of $CH_4$ and CO is still continuous. It is also noticeable that the efficiency of 15%-$V_2C$/g-$C_3N_4$ is much greater for the production of $CH_4$ than for CO during photocatalytic $CO_2$ reduction. This enhanced photocatalytic activity and photostability of the 15%-$V_2C$/g-$C_3N_4$ heterojunction is a result of the excellent interfacial interaction between g-$C_3N_4$ and $V_2C$ nanosheets and the efficient separation of charge carriers. As a result, the 15%-$V_2C$/g-$C_3N_4$ composite exhibits exceptional durability for continual CO and $CH_4$ generation in multiple cycles.

### *3.4. Spent catalyst analysis*

The reproducibility of the 2D/2D $V_2C$/g-$C_3N_4$ composite catalyst was further evaluated by measuring its ability to withstand repeated cycling under visible light for continuous photocatalytic $CO_2$ reduction to CO and $CH_4$. After three consecutive cycles of use, the spent catalyst was collected and examined using XRD, FTIR, and TGA in order to support stability of the photocatalysts. The interaction of the components in the spent 2D/2D $V_2C$/g-$C_3N_4$ nanocomposite has not been noticeably changed by XRD analysis, as shown in Fig. 16 (a). The spent catalyst is still maintaining similar XRD peaks to fresh peaks that appeared at 13.4°, 35.5°, 41.4°, 55.6°, 63.7°, 75°, and 79° were assigned to the crystal indices of (002), (101), (103), (106), (110), (109), and (116) of the delaminated $V_2C$ MXene. More significantly, there was no evidence of peaks shifting in the composite of 2D/2D $V_2C$/g-$C_3N_4$, which supports the catalyst's high stability for continuous photocatalytic $CO_2$ conversion to $CH_4$ and CO under visible light irradiations. As shown in Fig. 16 (b), the FTIR analysis of spent 2D/2D $V_2C$/g-$C_3N_4$ catalyst has dips at 805, 810, 885, 1233, 1337, 1401, 1415, 1559, 1630, 1638, 2354, 3000, and 3290 $cm^{-1}$. This reveals that the spent 2D/2D $V_2C$/g-$C_3N_4$ catalyst is still maintaining similar dips regarding the chemical bonds, and functional groups that could exist of fresh catalyst samples. This illustrates successful preparation with high stability of 2D $V_2C$, and 2D g-$C_3N_4$ in 2D/2D $V_2C$/g-$C_3N_4$ nanocomposite. Using thermogravimetric analysis (TGA), the purity and stability temperatures of the fresh and spent 2D/2D $V_2C$/g-$C_3N_4$ composite catalyst were determined; the results are depicted in Fig. 16(c). The thermal stability was evaluated by comparing the occurrences of weight loss across the temperature range. The fresh 2D/2D $V_2C$/g-$C_3N_4$ catalyst demonstrated the best coking resistance over the period of the reaction. The TGA curve of a fresh photocatalyst indicates that the nanocomposite is nonvolatile up to 500°C, even in the existence of airflow. A significant weight increase of 59.5% over the 2D/2D $V_2C$/g-$C_3N_4$ catalyst was observed at a high temperature of 500°C. The thermal stability is still also present even after 4 h of irradiation, as shown by the similar non-volatile and decomposition curve patterns in the TGA of the spent 2D/2D $V_2C$/g-$C_3N_4$ photocatalyst. The spent 2D/2D $V_2C$/g-$C_3N_4$ catalyst demonstrated coke resistance, with 66.3% of coke production starting at 400°C. This is due to the carbon content of g-$C_3N_4$ and $V_2C$ nanosheets. It is clear that moisture attaching to the catalyst surface is what caused the weight loss in the spent catalyst to start off higher than in the fresh sample. However, the TGA results clearly show that after 4 h of irradiation, no additional carbon was deposited on the spent 2D/2D $V_2C$/g-$C_3N_4$ composite during the photocatalytic $CO_2$ reduction process. Thus, it is proving that the 2D/2D $V_2C$/g-$C_3N_4$ composite excellent stability over three successive cycles. This also illustrates how well-suited it is for solar energy applications. All of these findings show that when exposed to visible light, the 2D/2D $V_2C$/g-$C_3N_4$ composite catalyst effectively reduced $CO_2$ to CO and $CH_4$. The total moles of carbon dioxide converted throughout the photocatalytic $CO_2$ reduction process would therefore be equal to the total moles of CO and $CH_4$ produced over the catalyst surface.

### *3.5. Performance analysis*

Although the rate of production (R) and selectivity (S) are critical parameters for evaluating the effectiveness of any photocatalytic system, these values do not provide information about the photon energy

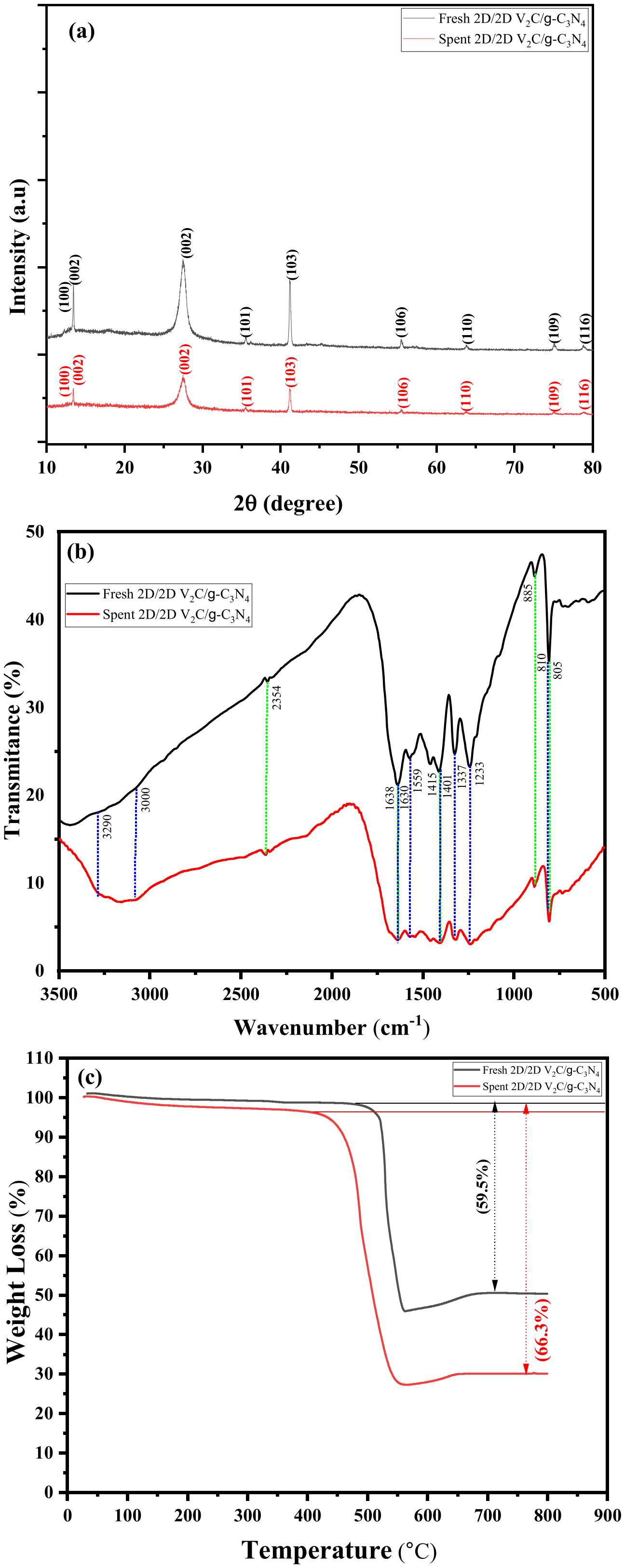

**Fig. 16.** (a) The XRD analysis of fresh and spent 2D/2D $V_2C$/g-$C_3N_4$ composite catalyst, (b) FTIR analysis of fresh and spent 2D/2D $V_2C$/g-$C_3N_4$ composite catalyst, (c) TGA analysis of fresh and spent 2D/2D $V_2C$/g-$C_3N_4$ composite catalyst.

consumed. The reason is that yields and selectivity would vary depending on light intensity, wavelength and catalyst loading [84]. Thus, instead of evaluating merely the production rate, all of these factors should be thoroughly examined. Recently, quantum efficiency is very important to evaluate different photo-catalytic systems by considering photon flux consumed and products obtained. Quantum yield is defined in heterogeneous photocatalysis as the ratio of production rate (mol/s) to photonic flux (mol/s) when a single photon produces a pair of electrons and holes. Photon energy is used to produce electrons and then consumed through the $CO_2$ reduction method, and the QYs delivers these details. The R, and S, and QYs for CO and $CH_4$ could be evaluated according to Eqs. (7)-(10), respectively [85].

$$R = \frac{mole\ of\ C_i\ in\ product}{Time\ (t)\ X\ Weight\ (W)} \tag{7}$$

$$S = \frac{C_i\ moles\ in\ product}{Total\ moles\ in\ C\ product} X100 \tag{8}$$

$$QYs = \frac{n_i X R_i}{Number\ of\ incident\ photons} X100 \tag{9}$$

$$Numberofincidentphotons = \frac{P\lambda St}{hc} \tag{10}$$

where C, $C_i$, t, and W represent to the total moles of carbon produced, express to species of mole carbon (CO, $CH_4$) in the mixture product, time (h), and weight of catalyst (mg), whereas P, λ, S, t, h, and c imply to the luminous intensity of incident light, wavelength of light, irradiated area of 25 $cm^2$, illumination time, Planck constant, and the speed of light, respectively. Sources of light 20 $mWcm^{-2}$, and QY calculations were conducted at a wavelength of 450 nm. The values of 2 and 8 electrons were utilized in the QY computation since they are consumed in CO and $CH_4$ production, respectively. The production rate and QY were determined using loading of photocatalyst at 50 mg, a source of light 20 mW $cm^2$, and a 4 h irradiation time.

The rate of production, selectivity, and QY of CO/$CH_4$ obtained following conversion of $CO_2$ with the $H_2O$ as reducing agent over pristine g-$C_3N_4$, 10 wt% $V_2AlC$/g-$C_3N_4$ and 15%-$V_2C$/g-$C_3N_4$ are summarized in Table 1. $CH_4$ was generated at a rate of 205 µmole g-$cat^{-1}$ over 15%-$V_2C$/g-$C_3N_4$ with a selectivity of 57.58%, which is 1.1 and 6.8-fold larger than when it was generated with 10% wt. $V_2AlC$/g-$C_3N_4$ and g-$C_3N_4$, respectively. Likewise, a generation rate of 151 µmole g-$cat^{-1}$was created for CO with a selectivity of 42.41%, that is 1.0 and 1.3-fold better than the selectivity achieved over 10 wt%$V_2AlC$/g-$C_3N_4$ and g-$C_3N_4$, respectively. The amount of QY for $CH_4$ yield over 15%-$V_2C$/g-$C_3N_4$ was 1.1 and 6.87 times higher than QY of 10 wt%$V_2AlC$/g-$C_3N_4$ and g-$C_3N_4$, respectively, whereas the amount of QY for CO yielded over 15%-$V_2C$/ g-$C_3N_4$ was 1.02 and 1.32 times higher than QY of 10 wt% $V_2AlC$/g-$C_3N_4$ and g-$C_3N_4$, respectively.

This is due to their excellent photoelectrical characteristics, high conductivity, and efficient absorption of visible light. Furthermore, the heterojunction structure may facilitate as well as provide adequate charge transfer, significantly speeding up the splitting and migration of high-activity charges created by photons.

The results of the photocatalytic $CO_2$ method over the 15%-$V_2C$/g-$C_3N_4$ nanosheets were then compared to those of other recent research on $CO_2$ and $H_2O$ over a variety of photocatalyst composites with a variety of reaction conditions, which are summarized in Table 2. The performance of a 15%-$V_2C$/g-$C_3N_4$ composite was compared to that of similar available literature, despite the fact that no literature exists on the use of $V_2C$ MXene for photocatalytic $CO_2$ reduction applications. Quantum yield and production rates were used to compare performance despite the fact that testing conditions varied across others literature. It was possible to obtain CO and $CH_4$ generation rates of 5.19 and 0.004 µmol $g^{-1}$ $h^{-1}$, respectively, using 2D $Ti_3C_2$ and g-$C_3N_4$, according to Yang and co-authors. The combined effect of boosted $CO_2$ adsorption and inhibited photoinduced charge recombination result in an increase in photocatalytic activity [86]. In another development, g-$C_3N_4$ loaded with alkalinized $Ti_3C_2$ MXene was examined for photocatalytic $CO_2$ reduction and discovered that the $Ti_3C_2$/MXene composite has a 5.9 fold increase in photoactivity for CO conversion when compared to pure g-$C_3N_4$ photocatalyst [23]. According to X. Zhao et al., the higher amounts of CO and $CH_4$ were obtained through $CO_2$ conversion within visible light using metal modified composites. When Pt and $CeO_2$ were mixed with 3D g-$C_3N_4$, CO and $CH_4$ were increased to 4.69 and 3.03 µmol $g^{-1}$ $h^{-1}$, respectively [87]. In another study under visible light, a $CH_4$ development rate of 0.99 µmol $g^{-1}$ $h^{-1}$ was attained among the MXene-based composites via $CO_2$ photoreduction over 2% $Ti_3C_2$ linked g-$C_3N_4$[88]. Controlled chemical and ultrasonic methods were used by Tahir et al. [44] to fabricate multilayer $Ti_3C_2$ nanosheets embedded with $TiO_2$ nanoparticles and anchoring with PCN. With selectivity of 80.16% and 19.84%, the greatest CO and $CH_4$ production rates were achieved over 10TiC-48/PCN, that were 306.75 and 60.15 µmol $g^{-1}$ $h^{-1}$, respectively. Therefore, for the conversion of $CO_2$ to CO and $CH_4$, $Ti_3C_2$ MXene based composites could be as effective as metal-modified g-$C_3N_4$ composites. In the current study, the external surface of $V_2C$ layers were uniformly covered with 2D g-$C_3N_4$, which acts as a mediator for electron transport between the composite materials. In comparison, the current work achieved remarkably improved photocatalytic $CO_2$ conversion to CO and $CH_4$ with high $CH_4$ production owing to the synergistic effect of 15%-$V_2C$/g-$C_3N_4$ and strong interfacial interaction with porous g-$C_3N_4$, which enables proficient charge carrier separation.

### 3.6. Proposed mechanism for photocatalytic $CO_2$ reduction

In the photocatalytic $CO_2$ reduction with $H_2O$ over the 15%-$V_2C$/g-$C_3N_4$ composite, the potential products were CO and $CH_4$. Fig. 17 depicts a proposed photocatalytic pathway for photocatalytic $CO_2$ conversion to CO and $CH_4$ production, which helps to explain why a 15%-$V_2C$/g-$C_3N_4$ composite catalyst performs better. The electronic band structure was first defined in order to investigate a potential mechanism for photocatalytic $CO_2$ reduction. As a result, the VB position was determined to be 1.67 eV and the CB position to be − 1.21 eV using Eqs. (2) and (3) with the bang gap energy of 2.88 eV for g-$C_3N_4$ [89]. The reaction pathways for better charge transport processes and their utilization in

**Table 1**
Summary of production rate, selectivity and quantum yields on different photocatalysts for $CH_4$ and CO generation.

| Catalyst | Generation rate[a] (µmol. $g^{-1}$) | | Selectivity[b] (%) | | Quantum Yield[c] (%) | | Apparent Quantum Yield (%) |
|---|---|---|---|---|---|---|---|
| | $CH_4$ | CO | $CH_4$ | CO | $CH_4$ | CO | |
| g-$C_3N_4$ | 30 | 114 | 20.83 | 79.16 | 0.112 | 0.105 | 0.215 |
| 10%$V_2AlC$+CN | 185 | 148 | 55.55 | 44.44 | 0.683 | 0.136 | 0.819 |
| 15% $V_2C$/CN | 205 | 151 | 57.58 | 42.41 | 0.756 | 0.139 | 0.895 |

[a] Calculated rate of generation based on a four-hour irradiation period and a 50 mg catalyst loading.
[b] On the basis of $CH_4$ and CO, the selectivity is estimated.
[c] Quantum yield was estimated using a light source of 20 $mWcm^{-2}$ and a wavelength of 420 nm.

**Table 2**
A review of recent advances in photocatalytic $CO_2$ reduction performance across a variety of photocatalyst composites.

| Name of photocatalyst | Method of Synthesis | photocatalyst Loading | Light Source Power Wavelength | Reactor Parameters | Product (s) (rate)μmol $g^{-1}$ $h^{-1}$ | Quantum Yields (QY) | Ref. |
|---|---|---|---|---|---|---|---|
| 10 wt% $V_2AlC$/ g-$C_3N_4$ | Following physical mixing, an ultrasonic technique is used. | 50 mg catalyst | Visible light 35 W Xe lamp 420 nm | Fixed -bed photoreactor system Temp. = 25°C, Press. = 0.3 bar, Vol. = 80 $cm^3$, Time = 4 h. | $CH_4$ = 185<br>CO = 148 | $CH_4$ = 0.683%<br>CO = 0.136% | Current study |
| 15%–48 h $V_2C$/ g-$C_3N_4$ | Physical mixing followed by an ultrasonic approach | 50 mg catalyst | Visible light 35 W Xe lamp 420 nm | Fixed-bed photoreactor system Temp. = 25°C, Press. = 0.3 bar, Vol. = 80 cm3, Time = 4 h, etching time = 48 h | $CH_4$ = 205<br>CO = 151 | $CH_4$ = 0.765%<br>CO = 0.139% | Current study |
| 2D/2D$Ti_3C_2$/g-$C_3N_4$ | directly calcining the mixture of multi-layered $Ti_3C_2$ particles and urea | 20 mg catalyst | 300 W Xenon lamp, Wavelength = 420 nm | – | $CH_4$ = 0.044<br>CO = 5.19 | – | [86] |
| Pt@$CeO_2$/ 3DCN | Calcination method and photoreduction technology | 100 mg catalyst | UV and visible light | Closed photochemical reactor, involving 100 mL of NaOH solution (0.1 M) and 1 mL of triethanolamine (TEOA) | $CH_4$ = 3.03<br>CO = 4.69 | – | [87] |
| 2% $Ti_3C_2$/g-$C_3N_4$ | simple one-step electrostatic self-assembly method | 15 mg catalyst | 300 W Xenon lamp, Wavelength = 420 nm | DI-water with a polytetrafluoroethylene inner tank in a 200 mL cylindrical steel reactor, Pressure = 0.6 MPa | $CH_4$ = 0.99 | | [88] |
| 10TiC-48/PCN | Ultrasonic approach | 150 mg catalyst | Light intensity = 20 mW/$cm^2$, Wavelength = 420 nm | Fixed-bed photoreactor, Reactor volume = 150 $cm^3$. | $CH_4$ = 64.25<br>CO = 394.03 | $CH_4$ = 1.089<br>CO = 1.669 | [44] |

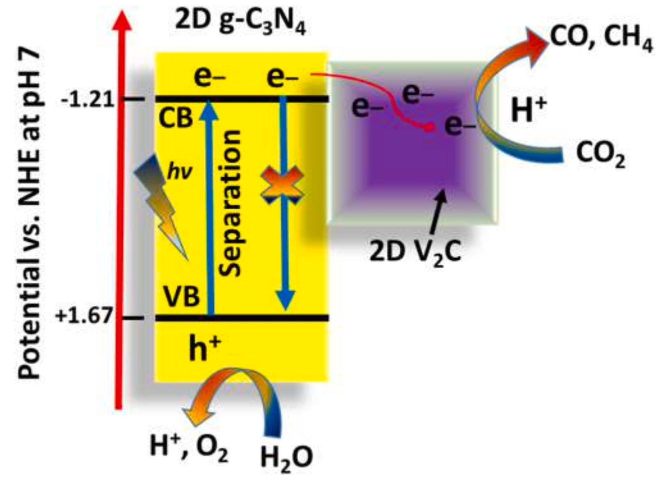

**Fig. 17.** Schematic illustration for charge carrier separation over the 15%-$V_2C$/ g-$C_3N_4$ composite under visible light for photocatalytic $CO_2$ reduction towards CO and $CH_4$ production.

the redox of $CO_2$ to form CO and $CH_4$ are shown in Eqs. (11)–(16).

**Step 1: Activation of Photocatalyst**

$$g-C_3N_4\xrightarrow{hv}g-C_3N_4(h^+)+g-C_3N_4(e^-) \tag{11}$$

$$g-C_3N_4(e^-)+V_2C\rightarrow g-C_3N_4+V_2C(e^-) \tag{12}$$

**Step 2: The reduction mechanism**

$$CO_2+e^-\rightarrow CO^{\cdot-} \tag{13}$$

**Step 3: The oxidation mechanism**

$$2H_2O+4h^+\rightarrow O_2+4H^+ \tag{14}$$

**Step 4: CO and $CH_4$ product development**

$$CO_2+2H^++2e^-\rightarrow CO+H_2O \tag{15}$$

$$CO_2+8H^++8e^-\rightarrow CH_4+2H_2O \tag{16}$$

When g-$C_3N_4$ was exposed to visible region, electrons were stimulated from the VB to the CB, leaving holes in the VB (Eq. (11)). This resulted in the generation of charges carriers ($e^-$ /$h^+$). Electrons from the CB of g-$C_3N_4$ successfully migrated to the conductive $V_2C$ because of its powerful electronic properties as indicated in Eq. (12). Due to the presence of $V_2C$ nanosheets and great contact with the g-$C_3N_4$ surface, $CO_2$ reduction and water oxidation are particularly effective. The electrons are being used to reduce $CO_2$ to its radical, as shown in Eq. (13). Likewise, holes are consumed in the formation of protons and oxygen, as seen in Eq. (14). CO and $CH_4$ were produced by involving 2 and 8 electrons and protons, respectively, as shown in Eqs. (15) and (16).

Furthermore, as stated in the literature, $V_2C$ could form a Schottky junction with another semiconductor, allowing for efficient electron flow in the composite [90]. The semiconductor's energy band bends upward to reach the Fermi level equilibrium, providing a Schottky barrier between the 2D g-$C_3N_4$ and 2D $V_2C$ MXene. The electrons in the CB of g-$C_3N_4$ have the potential to migrate toward $V_2C$ due to the difference in Fermi levels of g-$C_3N_4$ and $V_2C$, allowing for efficient charge separation [91]. Such a characteristic makes it possible for $V_2C$ to function as an "electron sink" for quickly and continuously receiving the photogenerated electrons from the CB of the 2D g-$C_3N_4$. The Schottky barrier also prevents photogenerated electrons from flowing backward, ensuring that the photogenerated charge carriers are separated spatially. The separation and migration of the charge carrier could be further facilitated by the synergistic interaction of 2D/2D $V_2C$/g-$C_3N_4$, which is advantageous for effective $CO_2$ conversion.

Thermodynamically, CO and $CH_4$ generation is possible because the conduction band (CB) location of g-$C_3N_4$ (−1.21 eV) is lower than the reduction potentials of $CO_2$/CO (−0.48 eV) and $CO_2$/$CH_4$ (−0.24 eV). Furthermore, because g-$C_3N_4$ has a higher positive VB (+1.67 V) than $H_2O$/$O_2$ (0.82 eV vs. SHE at pH = 7) and has been described in previous studies, g-$C_3N_4$ can oxidize $H_2O$ into $O_2$. As can be observed, producing $CH_4$ requires eight electrons and eight protons through the $CO_2$ conversion method, but producing CO requires only two electrons and two protons. Due to the quick recombination of photogenerated charges over pure g-$C_3N_4$, very poor photocatalytic $CO_2$ reduction with lower amounts of methane was achieved over g-$C_3N_4$. However, the 15%-$V_2C$/ g-$C_3N_4$ composite catalyst provided the most methane due to the combined benefits of $V_2C$ in avoiding rate of recombination and presenting various electron separation paths for photoreduction of $CO_2$ and CO to $CH_4$. This proves that the composite catalyst can efficiently produce electrons and protons, allowing for increased methane production when exposed to visible light. Thus, regulated preparation of a 2D/2D nanocomposite composed of 15%-$V_2C$/g-$C_3N_4$ with superior electron trapping and transport properties results in an excellent photocatalyst for photocatalytic generation when exposed to visible light.

## 4. Conclusions

To summarize, A new 2D/2D heterojunction of 15%− 48hV$_2$C/g-C$_3$N$_4$ composite was successfully fabricated using physical mixing followed by an ultrasonic method. It demonstrates a significant increase in photocatalytic CO$_2$ efficiency under visible light. Electrical conductivity in the V$_2$C MXene makes it a suitable cocatalyst. Consequently, coupling with another photocatalyst to increase the photoactivity is advantageous. The analysis of 15%− 48hV$_2$C/g-C$_3$N$_4$ composite demonstrates selective CH$_4$ production via CO$_2$-water reaction approach. CH$_4$ generation rate of 205 μmol g$^{-1}$ was achieved over 15%− 48hV$_2$C/g-C$_3$N$_4$, which is 1.1 and 6.7 folds higher than using 10 wt% V$_2$AlC/g-C$_3$N$_4$ and g-C$_3$N$_4$ samples, respectively. Similarly, highest CO production rate of 151 μmol g$^{-1}$ was achieved with CO$_2$-water system over 15%− 48 h V$_2$C/g-C$_3$N$_4$, which is 1.1 and 1.3 times than folds higher than using 10 wt% V$_2$AlC/ g-C$_3$N$_4$ and g-C$_3$N$_4$ samples, respectively. The CH$_4$ generation rate was 205 μmol g$^{-1}$ using CO$_2$-water system. More interesting, the CH$_4$ generation rate was enhanced to 254 μmol g$^{-1}$ using a CO$_2$-methanol–water system. This is 1.23 and 1.7 times more than the efficiency of CO$_2$-water and CO$_2$-hydrogen photocatalytic systems, respectively. Moreover, the effects of photocatalyst loading, reforming systems, and varying the pressure were also investigated. Theses parameters had an effective effect on determining the efficiency of the photocatalysts. This is owing to the effective separation of charge transfer and the enhanced sorption process on the multilayer surface. This selective photocatalytic conversion of Carbon dioxide to methane indicates that 15% -V$_2$C/g-C$_3$N$_4$ is an attractive material that should be further investigated for solar energy applications. The results of the stability test showed that CO and CH$_4$ are continuously evolving in photocatalytic cycles. These encouraging results and novel insights might be valuable for further exploration in this field for wastewater and solar energy applications.

## CRediT authorship contribution statement

**Mohamed Madi:** Methodology, Writing – original draft, Formal analysis. **Muhammad Tahir:** Financial support, Conceptualization, Supervision, Editing, Proof reading. **Zaki Yamani Zakaria:** Editing and Proof reading.

## Declaration of Competing Interest

The authors declare that they have no known competing financial interests or personal relationships that could have appeared to influence the work reported in this paper.

## Data availability

No data was used for the research described in the article.

## Acknowledgments

The authors would like to extend their deepest appreciation to University Technology Malaysia, Malaysia, for financial support of this work under the Research University Grant vot 21H66 and United Arab Emirates University (UAEU), UAE under Startup research grant vot no. 12N097.

## References

[1] R.R. Ikreedeegh, M. Tahir, A critical review in recent developments of metal-organic-frameworks (MOFs) with band engineering alteration for photocatalytic CO$_2$ reduction to solar fuels, J. CO$_2$ Util. 43 (2021), 101381.

[2] A. Francis, S. Shanmuga Priya, S. Harish Kumar, K. Sudhakar, M. Tahir, A review on recent developments in solar photoreactors for carbon dioxide conversion to fuels, J. CO$_2$ Util. 47 (2021), 101515.

[3] N. Shehzad, M. Tahir, K. Johari, T. Murugesan, M. Hussain, A critical review on TiO$_2$ based photocatalytic CO$_2$ reduction system: strategies to improve efficiency, J. CO$_2$ Util. 26 (2018) 98–122.

[4] M. Elavarasan, W. Yang, S. Velmurugan, J.-N. Chen, Y.-T. Chang, T.C.-K. Yang, T. Yokoi, In-situ infrared investigation of m-TiO$_2$/α-Fe$_2$O$_3$ photocatalysts and tracing of intermediates in photocatalytic hydrogenation of CO$_2$ to methanol, J. CO$_2$ Util. 56 (2022).

[5] Y.-T. Li, L. Zhou, W.-G. Cui, Z.-F. Li, W. Li, T.-L. Hu, Iron promoted MOF-derived carbon encapsulated NiFe alloy nanoparticles core-shell catalyst for CO$_2$ methanation, J. CO$_2$ Util. 62 (2022), 102093.

[6] B. Tahir, M. Tahir, N.A.S. Amin, Photo-induced CO$_2$ reduction by CH$_4$/H$_2$O to fuels over Cu-modified g-C$_3$N$_4$ nanorods under simulated solar energy, Appl. Surf. Sci. 419 (2017) 875–885.

[7] M. Tahir, N.A.S. Amin, Photo-induced CO$_2$ reduction by hydrogen for selective CO evolution in a dynamic monolith photoreactor loaded with Ag-modified TiO$_2$ nanocatalyst, Int. J. Hydrog. Energy 42 (23) (2017) 15507–15522.

[8] M. Tahir, Hierarchical 3D VO$_2$/ZnV$_2$O$_4$ microspheres as an excellent visible light photocatalyst for CO$_2$ reduction to solar fuels, Appl. Surf. Sci. 467–468 (2019) 1170–1180.

[9] X. Fan, L. Zhang, M. Wang, W. Huang, Y. Zhou, M. Li, R. Cheng, J. Shi, Constructing carbon-nitride-based copolymers via Schiff base chemistry for visible-light photocatalytic hydrogen evolution, Appl. Catal. B 182 (2016) 68–73.

[10] Y. Zhao, M. Que, J. Chen, C. Yang, MXenes as co-catalysts for the solar-driven photocatalytic reduction of CO$_2$, J. Mater. Chem. A 8 (46) (2020) 16258–16281.

[11] L.-f. Hong, R.-t. Guo, Y. Yuan, X.-y. Ji, Z.-s. Li, Z.-d. Lin, W.-g. Pan, Recent progress of two-dimensional MXenes in photocatalytic applications: a review, Mater. Today Energy 18 (2020), 100521.

[12] J. Pei, J. Yang, T. Yildirim, H. Zhang, Y. Lu, Many-body complexes in 2D semiconductors, Adv. Mater. 31 (2) (2019), 1706945.

[13] R. Hu, G. Liao, Z. Huang, H. Qiao, H. Liu, Y. Shu, B. Wang, X. Qi, Recent advances of monoelemental 2D materials for photoctalytic applications, J. Hazard. Mater. (2020), 124179.

[14] B. Tahir, M. Tahir, M.G.M. Nawawi, Highly stable 3D/2D WO$_3$/g-C$_3$N$_4$ Z-scheme heterojunction for stimulating photocatalytic CO$_2$ reduction by H$_2$O/H$_2$ to CO and CH$_4$ under visible light, J. CO$_2$ Util. 41 (2020), 101270.

[15] W. Yu, D. Xu, T. Peng, Constructing a stable 2D layered Ti$_3$C$_2$ MXene cocatalyst-assisted TiO$_2$/g-C$_3$N$_4$/Ti$_3$C$_2$ heterojunction for tailoring photocatalytic bireforming of methane under visible light, J. Mater. Chem. A 3 (39) (2015) 19936–19947.

[16] A.A. Khan, M. Tahir, A. Bafaqeer, Constructing a stable 2D layered Ti$_3$C$_2$ MXene cocatalyst-assisted TiO$_2$/g-C$_3$N$_4$/Ti$_3$C$_2$ heterojunction for tailoring photocatalytic bireforming of methane under visible light, Energy Fuels 34 (8) (2020) 9810–9828.

[17] B. Tahir, M. Tahir, M.G. Mohd Nawawi, Well-designed 3D/2D/2D WO3/Bt/g-C$_3$N$_4$ Z-scheme heterojunction for tailoring photocatalytic CO$_2$ methanation with 2D-layered bentonite-clay as the electron moderator under visible light, Energy Fuels 34 (11) (2020) 14400–14418.

[18] R.R. Ikreedeegh, M. Tahir, Indirect Z-scheme heterojunction of NH$_2$-MIL-125(Ti) MOF/g-C$_3$N$_4$ nanocomposite with RGO solid electron mediator for efficient photocatalytic CO$_2$ reduction to CO and CH$_4$, J. Environ. Chem. Eng. 9 (4) (2021), 105600.

[19] J. Fu, B. Zhu, C. Jiang, B. Cheng, W. You, J. Yu, Hierarchical porous O-doped g-C$_3$N$_4$ with enhanced photocatalytic CO$_2$ reduction activity, Small 13 (15) (2017), 1603938.

[20] M. Tahir, B. Tahir, 2D/2D/2D O-C$_3$N$_4$/Bt/Ti$_3$C$_2$T$_x$ heterojunction with novel MXene/clay multi-electron mediator for stimulating photo-induced CO$_2$ reforming to CO and CH$_4$, Chem. Eng. J. 400 (2020), 125868.

[21] J.-y. Tang, W.-g. Zhou, R.-t. Guo, C.-y. Huang, W.-g. Pan, Enhancement of photocatalytic performance in CO$_2$ reduction over Mg/g-C$_3$N$_4$ catalysts under visible light irradiation, Catal. Commun. 107 (2018) 92–95.

[22] M. Tahir, B. Tahir, M.G.M. Nawawi, M. Hussain, A. Muhammad, Cu-NPs embedded 1D/2D CNTs/pCN heterojunction composite towards enhanced and continuous photocatalytic CO$_2$ reduction to fuels, Appl. Surf. Sci. 485 (2019) 450–461.

[23] Q. Tang, Z. Sun, S. Deng, H. Wang, Z. Wu, Decorating g-C$_3$N$_4$ with alkalinized Ti$_3$C$_2$ MXene for promoted photocatalytic CO$_2$ reduction performance, J. Colloid Interface Sci. 564 (2020) 406–417.

[24] H. Wang, R. Zhao, H. Hu, X. Fan, D. Zhang, D. Wang, 0D/2D heterojunctions of Ti$_3$C$_2$ MXene QDs/SiC as an efficient and robust photocatalyst for boosting the visible photocatalytic NO pollutant removal ability, ACS Appl. Mater. Interfaces 12 (36) (2020) 40176–40185.

[25] G. Chen, R. Gao, Y. Zhao, Z. Li, G.I.N. Waterhouse, R. Shi, J. Zhao, M. Zhang, L. Shang, G. Sheng, X. Zhang, X. Wen, L.Z. Wu, C.H. Tung, T. Zhang, Alumina-supported CoFe alloy catalysts derived from layered-double-hydroxide nanosheets for efficient photothermal CO$_2$ hydrogenation to hydrocarbons, J. Adv. Mater. 30 (3) (2018), 1704663.

[26] Y. Guan, S. Jiang, Y. Cong, J. Wang, Z. Dong, Q. Zhang, G. Yuan, Y. Li, X. Li, A hydrofluoric acid-free synthesis of 2D vanadium carbide (V$_2$C) MXene for supercapacitor electrodes, 2D Mater. 7 (2) (2020), 025010.

[27] B. Wang, A. Zhou, F. Liu, J. Cao, L. Wang, Q. Hu, Carbon dioxide adsorption of two-dimensional carbide MXenes, J. Adv. Ceram. 7 (3) (2018) 237–245.

[28] J. Wang, P. Zhai, T. Zhao, M. Li, Z. Yang, H. Zhang, J. Huang, Laminar MXene-Nafion-modified separator with highly inhibited shuttle effect for long-life lithium–sulfur batteries, Electrochim. Acta 320 (2019), 134558.

[29] E. Lee, A. VahidMohammadi, B.C. Prorok, Y.S. Yoon, M. Beidaghi, D.-J. Kim, Room temperature gas sensing of two-dimensional titanium carbide (MXene), ACS Appl. Mater. Interfaces 9 (42) (2017) 37184–37190.

[30] T.P. Nguyen, D.M.T. Nguyen, H.K. Le, D.-V.N. Vo, S.S. Lam, R.S. Varma, M. Shokouhimehr, C.C. Nguyen, Q. Van Le, MXenes: applications in electrocatalytic, photocatalytic hydrogen evolution reaction and $CO_2$ reduction, J. Mol. Catal. 486 (2020), 110850.

[31] H. Wang, Y. Wu, X. Yuan, G. Zeng, J. Zhou, X. Wang, J.W. Chew, Clay-inspired MXene-based electrochemical devices and photo-electrocatalyst: state-of-the-art progresses and challenges, Adv. Mater. 30 (12) (2018), 1704561.

[32] A. VahidMohammadi, A. Hadjikhani, S. Shahbazmohamadi, M. Beidaghi, Two-dimensional vanadium carbide (MXene) as a high-capacity cathode material for rechargeable aluminum batteries, ACS Nano 11 (11) (2017) 11135–11144.

[33] E. Ghasali, Y. Orooji, A. Azarniya, M. Alizadeh, M. Kazem-zad, Production of $V_2C$ MXene using a repetitive pattern of $V_2AlC$ MAX phase through microwave heating of Al-$V_2O_5$-C system, Appl. Surf. Sci. 542 (2021), 148538.

[34] C. Ling, L. Shi, Y. Ouyang, Q. Chen, J. Wang, Transition metal-promoted $V_2CO_2$ (MXenes): a new and highly active catalyst for hydrogen evolution reaction, Adv. Sci. 3 (11) (2016), 1600180.

[35] G. Gao, A.P. O'Mullane, A. Du, 2D MXenes: a new family of promising catalysts for the hydrogen evolution reaction, ACS Catal. 7 (1) (2017) 494–500.

[36] N. Li, X. Chen, W.-J. Ong, D.R. MacFarlane, X. Zhao, A.K. Cheetham, C. Sun, Understanding of electrochemical mechanisms for $CO_2$ capture and conversion into hydrocarbon fuels in transition-metal carbides (MXenes), ACS Nano 11 (11) (2017) 10825–10833.

[37] B. Zhu, B. Cheng, J. Fan, W. Ho, J. Yu, g-$C_3N_4$-based 2D/2D composite heterojunction photocatalyst, Small Struct. 2 (12) (2021), 2100086.

[38] L. Cheng, Q. Chen, J. Li, H. Liu, Boosting the photocatalytic activity of $CdLa_2S_4$ for hydrogen production using $Ti_3C_2$ MXene as a co-catalyst, Appl. Catal. B 267 (2020), 118379.

[39] M.H. Tran, T. Schäfer, A. Shahraei, M. Dürrschnabel, L. Molina-Luna, U.I. Kramm, C.S. Birkel, Adding a new member to the MXene family: synthesis, structure, and electrocatalytic activity for the hydrogen evolution reaction of $V_4C_3T$ x, ACS Appl. Energy Mater. 1 (8) (2018) 3908–3914.

[40] D. Qin, Y. Zhou, W. Wang, C. Zhang, G. Zeng, D. Huang, L. Wang, H. Wang, Y. Yang, L. Lei, Recent advances in two-dimensional nanomaterials for photocatalytic reduction of $CO_2$: insights into performance, theories and perspective, J. Mater. Chem. A 8 (37) (2020) 19156–19195.

[41] H. Dong, X. Zhang, Y. Zuo, N. Song, X. Xin, B. Zheng, J. Sun, G. Chen, C. Li, 2D $Ti_3C_2$ as electron harvester anchors on 2D g-$C_3N_4$ to create boundary edge active sites for boosting photocatalytic performance, Appl. Catal. A 590 (2020), 117367.

[42] M. Lu, Q. Li, C. Zhang, X. Fan, L. Li, Y. Dong, G. Chen, H. Shi, Remarkable photocatalytic activity enhancement of $CO_2$ conversion over 2D/2D g-$C_3N_4/BiVO_4$ Z-scheme heterojunction promoted by efficient interfacial charge transfer, Carbon 160 (2020) 342–352.

[43] F. He, B. Zhu, B. Cheng, J. Yu, W. Ho, W. Macyk, 2D/2D/0D $TiO_2/C_3N_4/Ti_3C_2$ MXene composite S-scheme photocatalyst with enhanced $CO_2$ reduction activity, Appl. Catal. B 272 (2020), 119006.

[44] M. Tahir, B. Tahir, In-situ growth of $TiO_2$ imbedded $Ti_3C_2T_A$ nanosheets to construct PCN/$Ti_3C_2TA$ MXenes 2D/3D heterojunction for efficient solar driven photocatalytic $CO_2$ reduction towards CO and $CH_4$ production, J. Colloid Interface Sci. 591 (2021) 20–37.

[45] Q. Shan, X. Mu, M. Alhabeb, C.E. Shuck, D. Pang, X. Zhao, X.-F. Chu, Y. Wei, F. Du, G. Chen, Y. Gogotsi, Y. Gao, Y. Dall'Agnese, Two-dimensional vanadium carbide ($V_2C$) MXene as electrode for supercapacitors with aqueous electrolytes, Electrochem. Commun. 96 (2018) 103–107.

[46] Y. Chen, H. Yao, F. Kong, H. Tian, G. Meng, S. Wang, X. Mao, X. Cui, X. Hou, J. Shi, $V_2C$ MXene synergistically coupling FeNi LDH nanosheets for boosting oxygen evolution reaction, Appl. Catal. B 297 (2021), 120474.

[47] F.V. Bekun, A.A. Alola, S.A. Sarkodie, Toward a sustainable environment: Nexus between $CO_2$ emissions, resource rent, renewable and nonrenewable energy in 16-EU countries, Sci. Total Environ. 657 (2019) 1023–1029.

[48] Y. Liu, H. Xiao, W.A. Goddard III, Schottky-barrier-free contacts with two-dimensional semiconductors by surface-engineered MXenes, JACS 138 (49) (2016) 15853–15856.

[49] H. Hu, R. Zhao, X. Fan, J. Liu, Y. Nie, D. Wang, Preparation of a novel $V_2C$ mxene/g-$C_3N_4$ and its performance in plasma catalytic denitrification, E3S Web Conf. EDP Sci. (2021) 02068.

[50] N. Fajrina, M. Tahir, Monolithic Ag-Mt dispersed Z-scheme pCN-$TiO_2$ heterojunction for dynamic photocatalytic $H_2$ evolution using liquid and gas phase photoreactors, Int. J. Hydrog. Energy 45 (7) (2020) 4355–4375.

[51] Q. Deng, F. Zhou, B. Qin, Y. Feng, Z. Xu, Eco-friendly poly(vinyl alcohol)/delaminated $V_2C$ MXene high-k nanocomposites with low dielectric loss enabled by moderate polarization and charge density at the interface, Ceram. Int. 46 (17) (2020) 27326–27335.

[52] Z. Wang, X. Li, J. Zhou, P. Liu, Q. Huang, P. Ke, A. Wang, Microstructure evolution of V–Al–C coatings synthesized from a $V_2AlC$ compound target after vacuum annealing treatment, J. Alloy. Compd. 661 (2016) 476–482.

[53] A. Akhundi, A. Badiei, G.M. Ziarani, A. Habibi-Yangjeh, M.J. Muñoz-Batista, R. Luque, Graphitic carbon nitride-based photocatalysts: toward efficient organic transformation for value-added chemicals production, Mol. Catal. 488 (2020), 110902.

[54] Z. Wang, K. Yu, Y. Feng, R. Qi, J. Ren, Z. Zhu, $VO_2$(p)-$V_2C$(MXene) grid structure as a lithium polysulfide catalytic host for high-performance Li–S battery, ACS Appl. Mater. Interfaces 11 (47) (2019) 44282–44292.

[55] Y. Bai, P.-Q. Wang, J.-Y. Liu, X.-J. Liu, Enhanced photocatalytic performance of direct Z-scheme BiOCl–g-$C_3N_4$ photocatalysts, RSC Adv. 4 (37) (2014) 19456–19461.

[56] J. Liu, T. Zhang, Z. Wang, G. Dawson, W. Chen, Simple pyrolysis of urea into graphitic carbon nitride with recyclable adsorption and photocatalytic activity, J. Mater. Chem. 21 (38) (2011) 14398–14401.

[57] Y. Bi, M.F. Ehsan, Y. Huang, J. Jin, T. He, Synthesis of Cr-doped $SrTiO_3$ photocatalyst and its application in visible-light-driven transformation of $CO_2$ into $CH_4$, J. $CO_2$ Util. 12 (2015) 43–48.

[58] R. Thakur, A. VahidMohammadi, J. Moncada, W.R. Adams, M. Chi, B. Tatarchuk, M. Beidaghi, C.A. Carrero, Insights into the thermal and chemical stability of multilayered $V_2CTx$ MXene, Nanoscale 11 (22) (2019) 10716–10726.

[59] M. Wu, B. Wang, Q. Hu, L. Wang, A. Zhou, The synthesis process and thermal stability of $V_2C$ MXene, Materials 11 (11) (2018).

[60] Y. Kim, A. Gkountaras, O. Chaix-Pluchery, I. Gélard, J. Coraux, C. Chapelier, M. W. Barsoum, T. Ouisse, Elementary processes governing $V_2AlC$ chemical etching in HF, RSC Adv. 10 (42) (2020) 25266–25274.

[61] D. Huang, Y. Xie, D. Lu, Z. Wang, J. Wang, H. Yu, H. Zhang, Demonstration of a white laser with $V_2C$ MXene-based quantum dots, Adv. Mater. 31 (24) (2019), 1901117.

[62] Y. Cao, T. Wu, K. Zhang, X. Meng, W. Dai, D. Wang, H. Dong, X. Zhang, Engineered exosome-mediated near-infrared-II region $V_2C$ quantum dot delivery for nucleus-target low-temperature photothermal therapy, ACS Nano 13 (2) (2019) 1499–1510.

[63] X. Jiang, A.V. Kuklin, A. Baev, Y. Ge, H. Ågren, H. Zhang, P.N. Prasad, Two-dimensional MXenes: From morphological to optical, electric, and magnetic properties and applications, Phys. Rep. 848 (2020) 1–58.

[64] V.N. Khabashesku, J.L. Zimmerman, J.L. Margrave, Powder synthesis and characterization of amorphous carbon nitride, Chem. Mater. 12 (11) (2000) 3264–3270.

[65] B. Li, H. Song, F. Han, L. Wei, Photocatalytic oxidative desulfurization and denitrogenation for fuels in ambient air over $Ti_3C_2$/g-$C_3N_4$ composites under visible light irradiation, Appl. Catal. B 269 (2020), 118845.

[66] W. Luo, Y. Liu, F. Li, J. Huo, D. Zhao, J. Zhu, S. Guo, $H_2O_2$ assisted hydrothermal oxidation of partially etched vanadium carbides (MXene) and their electrochemical properties as anode for Li-ion batteries, Appl. Surf. Sci. 523 (2020).

[67] A.A. Khan, M. Tahir, Well-designed 2D/2D $Ti_3C_2T_{A/R}$ MXene coupled g-$C_3N_4$ heterojunction with in-situ growth of anatase/rutile $TiO_2$ nucleates to boost photocatalytic dry-reforming of methane (DRM) for syngas production under visible light, Appl. Catal. B 285 (2021), 119777.

[68] R.R. Ikreedeegh, M. Tahir, Facile fabrication of well-designed 2D/2D porous g-$C_3N_4$–GO nanocomposite for photocatalytic methane reforming (DRM) with $CO_2$ towards enhanced syngas production under visible light, Fuel 305 (2021), 121558.

[69] G.I. Rashed, H. Hu, R. Zhao, X. Fan, J. Liu, Y. Nie, D. Wang, M. Kheshti, Preparation of a novel $V_2C$ mxene/g-$C_3N_4$ and its performance in plasma catalytic denitrification, E3S Web Conf. 252 (2021).

[70] R.J. Liu, L.X. Yang, Y. Wang, H.P. Bu, H.J. Liu, C.L. Zeng, Characterization and electrochemical properties of submicro-sized orthorhombic $V_2C$ for Li-ion storage, J. Solid State Electrochem. 26 (3) (2022) 831–842.

[71] K. Kannan, K.K. Sadasivuni, A.M. Abdullah, B. Kumar, Current trends in MXene-based nanomaterials for energy storage and conversion system: a mini review, Catalysts 10 (5) (2020) 495.

[72] J. Michael, Z. Qifeng, W. Danling, Titanium carbide MXene: synthesis, electrical and optical properties and their applications in sensors and energy storage devices, Nanomater. Nanotechnol. 9 (2019) 1–9.

[73] C. Prasad, X. Yang, Q. Liu, H. Tang, A. Rammohan, S. Zulfiqar, G.V. Zyryanov, S. Shah, Recent advances in MXenes supported semiconductors based photocatalysts: properties, synthesis and photocatalytic applications, J. Ind. Eng. Chem. 85 (2020) 1–33.

[74] H. Hou, G. Shao, W. Yang, Recent advances in g-$C_3N_4$-based photocatalysts incorporated by MXenes and their derivatives, J. Mater. Chem. A 9 (24) (2021) 13722–13745.

[75] X. Chen, W.-g. Pan, R.-t. Guo, X. Hu, Z.-x. Bi, J. Wang, Recent progress on van der Waals heterojunctions applied in photocatalysis, J. Mater. Chem. A 10 (14) (2022) 7604–7625.

[76] L.-L. Tan, W.-J. Ong, S.-P. Chai, A.R. Mohamed, Photocatalytic reduction of $CO_2$ with $H_2O$ over graphene oxide-supported oxygen-rich $TiO_2$ hybrid photocatalyst under visible light irradiation: Process and kinetic studies, Chem. Eng. J. 308 (2017) 248–255.

[77] W.A.W. Abu Bakar, R. Ali, S. Toemen, Catalytic methanation reaction over supported nickel–ruthenium oxide base for purification of simulated natural gas, Sci. Iran. 19 (3) (2012) 525–534.

[78] S. Kaneco, Y. Shimizu, K. Ohta, T. Mizuno, Photocatalytic reduction of high pressure carbon dioxide using $TiO_2$ powders with a positive hole scavenger, J. Photochem. Photobiol. C 115 (3) (1998) 223–226.

[79] I.H. Tseng, W.-C. Chang, J.C.S. Wu, Photoreduction of $CO_2$ using sol–gel derived titania and titania-supported copper catalysts, Appl. Catal. B 37 (1) (2002) 37–48.

[80] X. Xiong, Y. Zhao, R. Shi, W. Yin, Y. Zhao, G.I.N. Waterhouse, T. Zhang, Selective photocatalytic $CO_2$ reduction over Zn-based layered double hydroxides containing tri or tetravalent metals, Sci. Bull. 65 (12) (2020) 987–994.

[81] M. Tahir, Construction of a stable two-dimensional MAX supported protonated graphitic carbon nitride (pg-$C_3N_4$)/$Ti_3AlC_2/TiO_2$ Z-scheme multiheterojunction system for efficient photocatalytic $CO_2$ reduction through dry reforming of methanol, Energy Fuels 34 (3) (2020) 3540–3556.

[82] B. Tahir, M. Tahir, N.A.S. Amin, Tailoring performance of La-modified $TiO_2$ nanocatalyst for continuous photocatalytic $CO_2$ reforming of $CH_4$ to fuels in the presence of $H_2O$, Energy Convers. Manag. 159 (2018) 284–298.

[83] A. Raza, H. Shen, A.A. Haidry, L. Sun, R. Liu, S. Cui, Studies of Z-scheme $WO_3$-$TiO_2$/$Cu_2ZnSnS_4$ ternary nanocomposite with enhanced $CO_2$ photoreduction under visible light irradiation, J. $CO_2$ Util. 37 (2020) 260–271.

[84] B. Tahir, M. Tahir, M.A.C. Yunus, A.R. Mohamed, M. Siraj, A. Fatehmulla, 2D/2D Mt/m-CN composite with enriched interface charge transfer for boosting photocatalytic $CO_2$ hydrogenation by $H_2$ to $CH_4$ under visible light, Appl. Surf. Sci. 520 (2020), 146296.

[85] S. Nahar, M. Zain, A.A.H. Kadhum, H.A. Hasan, M. Hasan, Advances in photocatalytic $CO_2$ reduction with water: a review, Materials 10 (6) (2017) 629.

[86] C. Yang, Q. Tan, Q. Li, J. Zhou, J. Fan, B. Li, J. Sun, K. Lv, 2D/2D $Ti_3C_2$ MXene/g-$C_3N_4$ nanosheets heterojunction for high efficient $CO_2$ reduction photocatalyst: dual effects of urea, Appl. Catal. B 268 (2020), 118738.

[87] X. Zhao, J. Guan, J. Li, X. Li, H. Wang, P. Huo, Y. Yan, $CeO_2$/3D g-$C_3N_4$ heterojunction deposited with Pt cocatalyst for enhanced photocatalytic $CO_2$ reduction, Appl. Surf. Sci. 537 (2021), 147891.

[88] J. Hu, J. Ding, Q. Zhong, Ultrathin 2D $Ti_3C_2$ MXene Co-catalyst anchored on porous g-$C_3N_4$ for enhanced photocatalytic $CO_2$ reduction under visible-light irradiation, J. Colloid Interface Sci. 582 (2021) 647–657.

[89] A. Ali Khan, M. Tahir, Constructing S-scheme heterojunction of CoAlLa-LDH/g-$C_3N_4$ through monolayer $Ti_3C_2$-MXene to promote photocatalytic $CO_2$ re-forming of methane to solar fuels, ACS Appl. Energy Mater. 5 (1) (2022) 784–806.

[90] Y. Wang, D. Shen, Y. Liang, Y. Zhao, X. Chen, L. Zhou, M. Zhang, J. Xu, X. Liu, E. Hu, L. Wang, R. Xu, Y. Tong, Emulation of multiple-functional synapses using $V_2C$ memristors with coexistence of resistive and threshold switching, Mater. Sci. Semicond. Process. 135 (2021), 106123.

[91] B. Anasori, M.R. Lukatskaya, Y. Gogotsi, 2D metal carbides and nitrides (MXenes) for energy storage, Nat. Rev. Mater. 2 (2) (2017) 16098.